의학박사 학위논문

Immunomodulatory Effect of Breast Cancer Cell-Derived Exosomes on Macrophage and Dendritic Cells

유방암세포유래 엑소좀의 대식세포 및 수지상세포 면역조절 효과에 관한 연구

2020년 2월

서울대학교 대학원

의과학과

YINJI PIAO

A Thesis of the Degree of Doctor of Philosophy

유방암세포유래 엑소좀의 대식세포 및 수지상세포 면역조절 효과에 관한 연구

Immunomodulatory Effect of Breast Cancer Cell-Derived Exosomes on Macrophage and Dendritic Cells

February 2020

The Department of Biomedical Sciences,

Seoul National University

College of Medicine

YINJI PIAO

ABSTRACT

Immunomodulatory Effect of Breast Cancer Cell-Derived Exosomes on Macrophage and Dendritic Cells

YINJI PIAO

Biomedical Sciences
The Graduate School
Seoul National University

Introduction: Cancer cell-derived exosomes known as the mediators of intercellular communications, are involved in tumor progress and metastasis by modulating tumor immunity. Nevertheless, the role of macrophages or dendritic cells stimulated by breast cancer cell-derived exosome in breast tumor progression and metastasis is not fully elucidated. In this study, we investigated the interaction of

breast cancer cell-derived exosomes with macrophages or dendritic cells, and analyzed the tumor immunity of macrophage and dendritic cells which stimulated by exosomes. We also analyzed the molecular mechanisms of exosome mediated breast cancer growth and metastasis using bioluminescent imaging and ultrasound-guided photoacoustic imaging.

Methods: The human and mouse triple negative breast cancer cell lines MDA-MB-231 and 4T1, mouse macrophage cell line Raw264.7 and mouse dendritic cell line DC2.4 were used. MDA-MB-231-CD63/RFP, 4T1-CD63/RFP cells were established using lentivirus expressing RFP-tagged CD63, which is a specific marker of exosomes. MDA-MB-231-Luc/GFP cells expressing both green fluorescence protein (GFP) and the firefly luciferase (Luc), RAW264.7/GFP cells and DC2.4/GFP cells expressing GFP were established using a lentiviral system. RFP-tagged exosomes secreted from MDA-MB-231-CD63/RFP or 4T1-CD63/RFP cells were isolated. The size of isolated exosomes was measured by NanoSight and specific exosomal marker proteins were assessed by Western blot. The intercellular transfer of RFP tagged exosomes

between cells was monitored by confocal microscopy. The effects of exosomes on cell proliferation, migration and invasive abilities were evaluated by MTT and Trans-well migration assays. The expression of genes associated with the anti-or pro-tumor immunity in the exosome-stimulated macrophage and dendritic cells were evaluated using RT-PCR, Western blot and flow cytometry. The xenograft tumor models were produced by injection with MDA-MB-231-Luc/GFP cells into the mammary gland of female Balb/c nude mice. Tumor progression and metastasis affected by exosomes were noninvasively monitored by bioluminescence imaging and ultrasound-guided photoacoustic imaging after intratumoral injection of anti-EGFR-GNs. Histologic examination of tissue was performed by H&E staining and immunostaining.

Result: RFP tagged exosomes taken up by breast cancer cells, macrophages and dendritic cells can be tracked by live-cell microscopy, macrophage and dendritic cells when took up exosomes were exhibited slightly elongated morphology. Exosomes significantly increased cell growth, migration and invasion abilities. Exosomes activated macrophages to M1 and M2 phenotypes, which

exhibited high expression of M1 marker (NOS2) and M2 markers (CD206, Arginase-1). Exosomes led to dendritic cell activation by inducing upregulation of co-stimulatory molecules CD40, CD80, and CD86, the chemokine receptor CCR7, and TNF-α. Primary tumor growth and metastasis promoted by exosomes and exosome-stimulated dendritic cell migration into lymph node were observed by bioluminescent imaging and ultrasound-guided photoacoustic imaging.

Conclusions: We monitored the interaction of RFP-tagged exosomes with macrophages and dendritic cells in real-time. Our data demonstrated breast cancer cell-derived exosomes mediate breast cancer progress by modulating the immune function of macrophage and dendritic cells. The bioluminescent imaging and ultrasound-guided photoacoustic imaging combined with GNs allowed for sensitive and longitudinal monitoring of tumor growth, metastasis and dendritic cell migration *in vivo.*

Key words: Triple-negative breast cancer, Exosome, Lymph node, Tumor metastasis, Macrophage, Dendritic cell, Ultrasound guided

Photoacoustic imaging, Gold nanorods (GNs)

Student Number: 2015-22409

CONTENTS

ABSTRACT ---------- I

LIST OF FIGURES ----------VII

LIST OF ABBREVIATIONS ----------VIII

Chapter 1 ----------1

Breast Cancer Cell-Derived Exosomes and Macrophage Polarization are Associated with Lymph node Metastasis

INTRODUCTION ---------- 2

MATERIALS AND METHODS ----------5

RESULTS ----------15

DISCUSSION ----------25

Chapter 2 ----------31

Noninvasive Photoacoustic Imaging of Dendritic Cell Stimulated with Breast Cancer Cell-Derived Exosomes

INTRODUCTION ----------32

MATERIALS AND METHODS ----------35

RESULTS ----------48

DISCUSSION ----------54

REFERENCES ----------71

ABSTRACT IN KOREAN ----------84

LIST OF FIGURES

Figure 1-1. Generation of stable MDA-MB-231 cells overexpressing the exosomal CD63-RFP fusion protein and analysis of purified RFP-tagged exosomes. ----------58

Figure 1-2. TNBC cell migration and proliferation is enhanced by TNBC cell-derived exosomes. ----------59

Figure 1-3. Induction of M1/M2 polarization by TNBC cell-derived exosomes in vitro and *in vivo*. ----------60

Figure 1-4. Noninvasive BLI and US-guided PAI of primary tumor growth and axillary LN metastasis promoted by cancer cell-derived exosomes in TNBC models. ---------- 62

Figure 1-5. Histological analysis of axillary LN metastasis promoted by cancer cell-derived exosomes in TNBC models. ------64

Figure 2-1. Generation of stable 4T1 cells expressing the exosomal CD63-RFP fusion protein and analysis of purified exosomes. --65

Figure 2-2. Analysis of biological changes of exosome-stimulated DC2.4 cells. ---------- 66

Figure 2-3. Analysis of in vitro US-guided PAI of GN-labeled DC2.4 cells. ---------- -- --68

Figure 2-4. US-guided PAI and histological analysis of exosome -stimulated and GN-labeled DC2.4 cell migration into LNs. ---------- 69

LIST OF ABBREVIATIONS

EXO: Exosome

TNBC: Triple negative breast cancer

CL: Cell lysate

LN: Lymph node

DC: Dendritic cell

GNs: Gold nanorods

Anti-EGFR-GNs: antibody-conjugated gold nanorods

PAI: Photoacoustic imaging

US: Ultrasound

BLI: Bioluminescence imaging

Chapter 1

Breast Cancer Cell–Derived Exosomes and Macrophage Polarization are Associated with Lymph node Metastasis

INTRODUCTION

Axillary lymph node (LN) status, one of the first signs of metastatic spread, is an independent prognostic factor for all subtypes of breast cancer [1]. Triple-negative breast cancer (TNBC), which is characterized by the absence of the estrogen (ER) and progesterone (PR) receptors and the human epidermal growth factor receptor 2 (HER2), is the most aggressive breast cancer subtype and has a poor prognosis [2]. Evidence from previous clinical studies indicate that axillary LN metastasis develops in 50% of TNBC patients, and 70% to 80% of breast cancer patients with LN metastasis experience recurrence or distant metastasis develops [3, 4]. However, the underlying mechanisms of the LN metastatic process of TNBC remain to be further explored.

Exosomes are extracellular vesicles released from various cell types and contain numerous molecular constituents of the original cells, including proteins and nucleic acids. Exosomes facilitate disease progression and cell-to-cell communication [5]. Cancer cells secrete a large number of exosomes compared with non-transformed cells [6]. Exosomes released from cancer cells

stimulate cancer cell growth and mobility and the immune cell response in promoting cancer progression and metastasis [7, 8]. The pathological function of cancer-derived exosomes in cancer progression and metastasis includes modifying the immune cell response at both local and distant sites.

Macrophage polarization is a process by which macrophages express different functions in response to microenvironment signals and is a factor in tumor-suppressive or tumor-promoting immunity [9]. In the primary tumor and metastatic sites, tumor-associated macrophages are the most abundant immune cells. Macrophages exhibit different phenotypes, including classically activated macrophages (M1) or alternatively activated macrophages (M2), depending on the tumor type and stromal interactions [10, 11]. M1-type macrophages are inflammatory or anti-tumorigenic, based on the expression of inducible NO synthase (NOS2), whereas M2-type macrophages are anti-inflammatory and pro-tumorigenic based on the increased expression of CD206 and Arginase-1 [12]. An increase in M2-type macrophages is a prognostic marker for poor prognosis and metastasis in diverse cancer types [13-15]. Macrophages exhibit different properties in different subtypes of

breast cancer. Macrophages activated by co-culture with TNBC cells upregulate CD206, a commonly used marker of M2-type macrophages, compared with cells activated by ER breast cancer cells [16], suggesting that TNBC-exposed macrophages are more likely to exhibit M2 properties.

Studies suggest that cancer-derived exosomes can reprogram the macrophage phenotype to provide a favorable microenvironment for tumor growth and dissemination in diverse cancers [17-22]. However, little is known about the relation among cancer-derived exosome, macrophage polarization, and LN metastasis in TNBC. We generated TNBC cells that produced exosomes tagged with a red fluorescence protein (RFP) reporter gene to visualize and track cancer exosomes, and we used noninvasive bioluminescent imaging (BLI) and ultrasound (US)-guided photoacoustic imaging (PAI) to monitor tumor growth and axillary LN metastasis in orthotopic TNBC models. We investigated whether TNBC exosome-related macrophage polarization promotes LN metastasis.

MATERIALS AND METHODS

Cell culture and antibody reagents

The human TNBC cell line (MDA-MB-231) and murine macrophage (Raw264.7) were obtained from the Korean Cell Line Bank (Seoul, Korea). All cells were grown in Roswell Park Memorial Institute (RPMI) 1640 medium (WelGENE, Daegu, Korea) containing 10% fetal bovine serum (FBS) and supplemented with a 1% antibiotic solution containing penicillin and streptomycin (Thermo Fisher Scientific, Waltham, MA, USA). Cells were cultured in a 5% CO2 incubator at 37° C. The primary antibodies used in this study were anti-cytokeratin 8/18/19 antibody, anti-GFP antibody, anti-RFP antibody, anti- CD63 antibody, anti- Alix antibody, and anti-Calnexin antibody, purchased from Abcam (Cambridge, MA, USA). Anti-NOS2 antibody, anti-CD206 antibody, anti- Arginase-1 antibody, and anti-GAPDH antibody were purchased from Santa Cruz Biotechnology (Dallas, Texas, USA). Anti-β-actin antibody was purchased from Sigma (St. Louis, MO, USA).

Exosome isolation and characterization

A stable MDA-MB-231/CD63-RFP cell line overexpressing the

exosomal CD63-RFP fusion protein was generated for monitoring RFP-tagged exosomes. Conditioned media were obtained from MDA-MB-231/ CD63-RFP grown at sub-confluence for 3 to 4 days in growth media containing serum depleted of bovine exosomes (Gibco Laboratories, Carlsbad, CA, USA). For isolation of exosomes from conditioned media, the Exo-spin Exosome Purification kit was used according to the manufacturer's instructions (Cell Guidance Systems, Cambridge, UK). Purified exosomes were then stored at -80° C until use.

Imaging of exosome transfer in cultured cells

For imaging of RFP-tagged exosome transfer in co-culture, MDA-MB-231/GFP (green fluorescence protein-tranduced MDA-MB-231) cells, RAW264.7/GFP (GFP-transduced RAW264.7) cells, and MDA-MB-231/ CD63-RFP cells were mixed (1:1) and cultured for 72 hours. Real-time imaging of RFP-tagged exosome transfer from MDA-MB-231/CD63-RFP cells to MDA-MB-231/ GFP cells or RAW264.7/GFP cells was performed by use of a laser scanning confocal microscope (Leica, Wetzlar, Germany). To visualize RFP-tagged exosome uptake by MDA-MB-231/GFP cells or

RAW264.7/GFP cells, isolated exosomes were resuspended in phosphate buffered saline (PBS) and quantified by use of the Pierce micro-BCA protein assay kit (ThermoScientific, Waltham, MA, USA). After administration of 10 μg of exosomes into cultured MDA-MB-231/GFP cells or RAW264.7/GFP cells, the cellular uptake of RFP-tagged exosomes was monitored by use of a laser scanning confocal microscope (Leica, Wetzlar, Germany).

Wound-healing assay

To assess the effect of exosomes on MDA-MB-231 cell migration, wound-healing assays were performed. MDA-MB-231 cells were seeded in a 12-well plate. When the cells formed a confluent monolayer, a scratch was generated by use of a micropipette tip, and cells were washed with PBS to remove cell debris. Purified exosomes (5-50 μg/mL) were added to MDA-MB-231 cells, and wound healing was monitored by photography. Images were obtained by use of a light microscope attached to a CCD camera (Leica, Wetzlar, Germany).

Proliferation assay

To investigate the effect of exosomes on MDA-MB-231 and

RAW264.7 cell proliferation, 1×10^4 cells were seeded in a 96-well plate and incubated in exosome-depleted FBS media for 24 hours. The purified exosomes (5-50 μg/mL) were administered to cultured cells for 24 hours to 48 hours. The cell proliferation rate was quantified by use of the 3-(4,5-dimethylthiazol-2-yl)- 2,5-diphenyltetrazolium bromide) (MTT) assay, and 10 μL of MTT reagent (5 mg/mL) were added to each well and incubated for 1 hour at 37° C. Formazan crystals were solubilized by the addition of 150 μL of dimethyl sulfoxide to each well. The optical density at 540 nm was measured by use of a microplate reader (GE Healthcare, Piscataway, NJ, USA), and the cell proliferation rate was determined.

Trans-well migration assay

To investigate the effect of exosomes on RAW264.7 cell migration, trans-well migration assays were performed, 1×10^5 Raw264.7 cells were deposited in the upper chamber of the trans-well plate with a 0.4- μm pore size (BD Bioscience, San Jose, CA, USA). The lower chamber was filled with 500 μL of serum-free medium with purified exosomes (5-50 μg/mL), and cells were incubated for 24 hours to 48 hours. Migrated cells were fixed in 4% paraformaldehyde

and stained with crystal violet, and the stained images were captured by light microscope. Crystal violet from the stained membrane was finally extracted with 1% sodium dodecyl sulfate (SDS). The optical density at 550 nm was measured by use of a microplate reader (GE Healthcare, Piscataway, NJ USA), and cell migration was determined.

Real-time RT-PCR

Total RNA was isolated by use of TRIzol Reagent (Invitrogen, Carlsbad, CA, USA) and was reverse-transcribed by use of random hexamers and Superscript III reverse transcriptase. Real-time PCR reactions were run on an ABI PRISM 7900 utilizing a SYBR Green PCR master mix (Applied Biosystems, Foster City, CA, USA). Results were analyzed by the ΔCt method, which reflects the threshold difference between a target gene and β-actin in each sample.

Western blot

Cells were lysed in RIPA buffer (Sigma, St. Louis, MO, USA). Proteins were separated by use of SDS-polyacrylamide gel electrophoresis (SDS-PAGE) and transferred to nitrocellulose membranes. The membranes were blocked by 5% skim milk in Tris-

buffered saline containing 0.05% Tween-20 and were incubated overnight at 4° C with primary antibodies. Membranes were incubated with HRP-conjugated secondary antibodies (Santa Cruz Biotechnology, Dallas, Texas, USA). The blotted membranes were visualized by use of enhanced chemiluminescence reagents (GE Healthcare, Danderyd, Sweden).

Immunocytochemistry

Cells were fixed in 2% paraformaldehyde and blocked by 2% bovine serum albumin. Cells were incubated with the primary antibodies for CD206 and NOS2 for 1 hour at 4° C followed by incubation with an appropriate secondary antibody for 30 minutes. Proteins were visualized with 3,3-diaminobenzidine, and hematoxylin was used as counterstain. The images were acquired by use of a microscope equipped with a CCD camera (Leica, Wetzlar, Germany).

Animals and orthotopic breast tumor models

Female BALB/c nude mice, 5 to 6 weeks old (Orient Bio, Sungnam, Korea), were housed in the animal care facility of the Biomedical Research Institute of Seoul National University Hospital. Animal care and experimental procedures were performed in accordance with

guidelines on the ethical use of animals that were approved by the Institutional Animal Care and Use Committee of Seoul National University Hospital (12-0353-C2A0). A total of 19 female Balb/c nude mice were used for BLI and US-guided PAI and histological studies. For exploration of the microenvironment modifications of axillary LN by tumor exosomes, healthy mice were assigned to two groups: PBS (n = 3) and exosomes (n = 3).

Approximately 1×10^6 viable cells were injected into the right fat pad of the first mammary gland. Tumor volume was measured with digital calipers and US imaging by use of a modified ellipsoidal formula for volume (volume = 1/2[length×width2]) [23]. Tumor-bearing mice injected with MDA-MB-231/Luc-GFP cells were randomly assigned to two groups: PBS (control) (n = 6) and exosome (n = 7). To investigate the function of tumor exosomes during tumor progression, purified RFP-tagged exosomes (10 μg) were administered via 10 repeated intravenous injections at 2-day intervals the day after tumor cell injection, and noninvasive imaging of tumor growth and LN metastasis followed by BLI and US-guided PAI were performed.

BLI and US-guided PAI

In vivo BLI, after intraperitoneal injection of 150 ng/ kg D-luciferin (Promega, San Luis Obispo, CA, USA), was conducted on the IVIS luminal II system (Caliper, Hopkinton, MA, USA). The sum of all detected photon counts within an oval-shaped region of interest (ROI), either primary tumor or axillary LN, was quantified in units of mean photons per second per centimeter squared per steradian (p/s/cm2/sr) by Living Image software. Anti-EGFR-GNs were purchased from Nanopartz, Inc. (Loveland, CO, USA). Before and 4 hours to 24 hours after intratumor injection of anti-EGFR-GNs (7.7 mg/kg GN), serial follow-up US-guided PAI of primary tumors and axillary LNs was performed in B mode and PA mode on a preclinical Vevo2100 LAZR imaging system (FUJIFILM VisualSonics Inc., Toronto, Ontario, Canada) equipped with a 40-MHz linear array transducer. The laser was tuned to optical wavelengths from 750 to 850 nm with a PA signal gain of 40 dB. The relative PA signal amplitude on image slices of tumor was quantified by post-processing software tools (FUJIFILM VisualSonics Inc., Toronto, Ontario, Canada) [24].

Histological analysis

The excised primary tumors and axillary LNs were fixed with 4% buffered formalin and embedded in paraffin blocks. Tissues were sectioned into 4-μm thick sections. Paraffin sections were deparaffinized in xylene and rehydrated in a series of graded ethanol and water solutions. For evaluation of anti-EGFR-GN accumulation, immunostaining, and immune gold-silver staining (Sigma, St. Louis, MO, USA) were performed according to the manufacturer's protocols. Hematoxylin and eosin (H&E) staining was performed to evaluate the change in cell and tissue structure. For immunostaining, deparaffinized sections were immersed in 0.01 M sodium citrate buffer (pH 6.0) and blocked by incubation with 0.1 M NH4Cl/PBS solution and 5% normal goat serum (Gibco Laboratories, Carlsbad, CA, USA) for 30 minutes. After incubation with primary antibodies for CK8/18/19, EGFR, GFP, CD63, NOS2, and CD206 and secondary antibodies directly conjugated with HRP, the sections were visualized with a peroxidase substrate kit (SK-4100; Vector Laboratories, Burlingame, CA, USA) and counterstained with hematoxylin solution (Millipore Ltd., Darmstadt, Germany). Histological images of stained tissues were acquired by use of a microscope equipped with a CCD

camera (Leica, Wetzlar, Germany). Seven fields at 40 × magnification within each section were randomly selected, and immunostained cells were quantified as the percentage of total cells in each area by Leica QWin image-analysis and image-processing software.

Statistical analysis

Results are expressed as the mean ± standard deviation (S.D.) and statistically evaluated by use of the two-tailed unpaired t test. A P-value less than 0.05 was considered statistically significant. Statistical analyses were performed by GraphPad Prism 5.0 (GraphPad Software, Inc., La Jolla, CA, USA).

RESULTS

Establishment of MDA-MB-231 cells expressing CD63-RFP and analysis of RFP-tagged exosomes

The tetraspanin CD63 protein is a common exosomal biomarker. To directly image breast cancer- derived exosomes, we established a MDA-MB-231/CD63- RFP cell line that stably expresses CD63-RFP protein (Figure 1-1A). Confocal fluorescence images revealed RFP-tagged exosomes purified from culture supernatant of MDA-MB-231/CD63-RFP cells (Figure 1-1B). NanoSight results revealed that MDA-MB-231/CD63-RFP cells released exosomes with heterogeneous sizes ranging from 3 to 200 nm in diameter (Figure 1-1C). Western blot revealed that purified exosomes exhibited high expression of specific exosomal marker proteins, such CD63 and Alix, but not the endoplasmic reticulum membrane marker Calnexin (Figure 1-1D).

TNBC cell-derived exosomes promote TNBC cell migration and proliferation

To visualize the intercellular transfer of exosomes between breast cancer cells, we performed live cell imaging performed using confocal

laser scanning microscopy. Figure 1-2A shows that RFP-tagged exosomes derived from MDA-MB-231/CD63-RFP cells were translocated into MDA-MB-231/GFP cells under direct co-culture with MDA-MB-231/CD63-RFP cells for 24 hours (Figure 1-2A). Figure 1-2B depicts the internalization of RFP-tagged exosomes in MDA-MB-231/GFP cells 24 hours after treatment with 10 μg/mL of RFP-tagged exosomes isolated from MDA-MB-231/CD63-RFP cells.

We investigated the effects of exosomes on MDA-MB-231 cell migration and proliferation. MDA-MB-231 cell migration was promoted by the administration of their secreted RFP-tagged exosomes (5-50 μg/mL) in a time-dependent manner (Figure 1-2C). MDA-MB-231 cell proliferation at 48 hours was enhanced in the RFP-tagged exosome-treated group (219.4 $\pm$ 2.538, P = 0.0214; 227.4 $\pm$ 1.466, P = 0.001; and 229.2 $\pm$ 0.984, P = 0.0004 at 10, 30, and 50 μg/mL, respectively) compared with the control group (208.4 $\pm$ 1.624) (Figure 1-2D).

TBNC cell-derived exosomes promote the migration and M2 polarization of macrophages *in vitro* and *in vivo*

To image exosomes transferred from cancer cells to macrophages, we performed direct co-culture of MDA-MB-231/CD63-RFP cells and macrophage RAW264.7 cells. Live images of RFP-tagged exosomes taken up by RAW264.7 cells were captured by confocal laser scanning microscopy. As shown in Figure 1-3A, most of the RAW264.7/GFP cells took up RFP-tagged exosomes and exhibited slightly elongated morphology after co-culture with MDA-MB-231/CD63-RFP cells for 24 hours.

Macrophage proliferation and migration, which promote the immune response, were evaluated by MTT assay and trans-well migration assay. Macrophage growth is not suppressed after treatment with 5 or 10 μg/mL exosomes, implying that cancer-derived exosomes exert low cytotoxic effects, but the administration of 30 or 50 μg/mL exosomes for 48 hours reduced macrophage growth (76.93 $\pm$ 0.53, P = 0.0013 or 74.80 $\pm$ 2.37, P = 0.0016) (Figure 1-3B). Figure 1-3C is an image of crystal violet staining of migrated RAW264.7 cells treated with different doses of RFP-tagged exosomes (5-50 μg/mL). The administration of low doses (5-10 μg/mL) of RFP-tagged exosomes for 24 hours or 48 hours resulted in an approximate 1.5-fold to 2-fold increase in

macrophage migration (166.14 ± 1.73 or 146.31 ± 1.05 versus 100.0 ± 0.73, $P < 0.0001$, 24 hours and 273.82 ± 8.52 or 304.49 ± 9.61 versus 137.74 ± 2.14, $P \leq 0.0001$, 48 hours) compared with untreated cells, whereas treatment with 30 to 50 μg/ mL RFP-tagged exosomes did not influence macrophage migration (Figure 1-3C), indicating that the growth-inhibitory and low migration-promoting effects of 30 to 50 μg/mL exosomes are caused by the cytotoxicity.

To evaluate M1 and M2 polarization of RAW264.7 cells treated with TNBC cell-derived exosomes, we investigated the expression of M1 (NOS2) and M2 (CD206, Arginase-1) markers. In trans-well co-culture with RAW264.7 and MDA-MB-231/CD63-RFP cells, we observed that CD206 staining intensity in RAW264.7 cells increased compared with NOS2 cells (Figure 1-3D). After 24 to 48 hours of treatment with 10 μg/mL RFP-tagged exosomes, which does not cause cytotoxic effects in RAW264.7 cells, Arginase-1, CD206, and NOS2 protein levels increased as compared with those of PBS-treated RAW264.7 cells (Figure 1-3E). In quantitative RT-PCR analysis, the administration of RFP-tagged exosomes (10 μg/mL) for 24 hours resulted in an increase in mRNAs expression of

Arginase-1 (11.0 ± 0.3.67, P = 0.036), CD206 (1.89 ± 0.08, P = 0.0037), and NOS2 (7.29 ± 1.53, P = 0.0028) compared with those of PBS-treated RAW264.7 cells (Figure 1-3F).

We examined in vivo M1 or M2 polarization in axillary LNs of non-tumor-bearing mice injected with TNBC cell-derived exosomes. M1 polarization marker (NOS2) expression was not detected, whereas M2 polarization marker (CD206) expression was detected in axillary LNs exhibiting CD63 (exosomal marker) at 3 hours after the injection with RFP-tagged exosomes (Figure 1-3G). The CD63-positive areas in PBS-injected LNs and exosome-injected LNs were 0.57% ± 0.17% and 2.80% ± 0.53%, respectively. The CD206-positive areas in PBS-injected LNs and exosome-injected LNs were 0.77% ± 0.38% and 5.65% ± 0.41%, respectively (Figure 1-3H).

Intravenous injection of TNBC cell-derived exosomes promotes axillary LN metastasis in orthotopic breast cancer models

To investigate the effect of cancer-derived exosomes on breast tumor progression and metastasis, we noninvasively monitored primary tumor growth and LN metastasis in mice after intravenous injection of RFP-tagged exosomes (10 μg, 10 injections at 2-day

intervals) using BLI and US-guided PAI (Figure 1-4A). BLI signals gradually increased in both PBS-injected and exosome-injected tumors (Figure 1-4B), and quantitative photon fluxes of primary tumors increased in exosome-injected mice ($7.03 \pm 1.97 \times 10^6$ p/s/cm2/sr) compared with PBS-injected mice ($2.06 \pm 0.95 \times 10^6$ p/s/cm2/sr) at 6 weeks after inoculation ($P = 0.0343$, Figure 1-4C). We noted no differences in average tumor volumes and BLI signals between PBS-injected mice and exosome-injected mice at 4 weeks (Figure 1-4C). However, at 4 weeks after inoculation, BLI signal ($9.46 \pm 0.1 \times 10^4$ p/s/cm2/sr) in the area of axillary LN metastasis can be detected in 2 of 7 exosome-injected mice, whereas the BLI signal was not detected in the axillary LNs of PBS-injected mice (Figure 1-4D and 1-4E).

Anti-EGFR-GNs are an active PAI contrast agent that selectively binds to EGFR-positive tumor cells in primary tumor mass and regional metastatic LN [25]. To noninvasively detect EGFR-positive tumors with axillary LN metastasis in mice after the intratumoral injection of anti-EGFR-GNs, we performed US-guided PAI. The representative US-guided PAIs of PBS-injected or exosome-

injected primary tumors before and 4 hours and 24 hours after the injection of anti-EGFR-GNs (7.7 mg/ kg) into primary tumors at 6 weeks are presented in Figure 1-4F. We detected strong PAI signals on the periphery of primary tumors in PBS-injected or exosome-injected mice up to 24 hours after injection of anti-EGFR-GN, we noted no differences in average PA signals in the primary tumor area of PBS-injected and exosome-injected mice (Figure 1-4G). The serial follow-up US-guided PAIs of axillary LNs in PBS-injected or exosome-injected mice are presented in Figure 1-4H. Average PAI signals in axillary LNs of exosome-injected mice at 4 hours and 24 hours increased compared with PBS-injected mice (1.46 ± 0.45 AU versus 0.31 ± 0.05 AU, P = 0.037 and 1.43 ± 0.19 AU versus 0.25 ± 0.03 AU, P = 0.0003) (Figure 1-4I). Based on *in vivo* US-guided PAI analysis, enhanced PAI signals in the axillary LNs in 5 of 7 exosome-injected mice and in 1 of 6 PBS-injected mice indicated that axillary LN metastasis increased on cancer exosome injection. Ex vivo results of US-guided PAI and confocal GFP fluorescence microscopy images of axillary LN dissections were consistent with *in vivo* imaging analysis (Figure 1-4J and 1-4K).

Histological analysis of axillary LNs correlated with anti-EGFR-

enhanced PAI signals in PBS-injected or exosome-injected mice

To verify the presence of anti-EGFR-GNs, which selectively target MDA-MB-231 cells, we performed silver staining in axillary LNs of tumor-bearing mice. As shown in Figure 1-5A, large numbers of anti-EGFR-GNs accumulated in the cortex of axillary LNs in 5 of 7 exosome-injected mice, but we observed anti-EGFR-GNs accumulation in axillary LNs in only 1 of 6 PBS-injected mice. The silver staining results were positive in all cases with *in vivo* PAI signals over 0.8 AU.

To confirm MDA-MB-231/Luc-GFP cell metastases in axillary LNs, we performed immunostainings for EGFR, cytokeratin 8/18/19 (CK8/18/19), and GFP. We observed strong immunostainings for EGFR, CK8/18/19, and GFP in the cortex zone of all axillary LNs of the exosome-injected group, but we observed minimal or no staining in most axillary LNs of the PBS-injected group (Figure 1-5B). Based on CK8/18/19 and EGFR immunostaining analysis, we detected axillary LN metastases in 6 of 7 exosome-injected mice and 2 of 6 PBS-injected mice.

TNBC cell exosome-promoted axillary LN metastasis is associated

with an increased ratio of M2/M1 polarized macrophages

We examined the presence of TNBC cell- derived exosomes using antibodies for the detection of human CD63 in axillary LNs of tumor-bearing mice (Figure 1-5C). We observed increased CD63 expression in the cortex area of LNs of exosome-injected mice (6.75% ± 1.18%) compared with LNs of PBS-injected mice (0.53% ± 0.22%) (P = 0.0001) (Figure 1-5D), suggesting that cancer exosomes are involved in creating a microenvironment favorable to LN metastasis. We investigated the differential macrophage polarized phenotypes in metastatic LNs via CD206 (M2 marker) and NOS2 (M1 marker) immunostaining. As shown in Figure 1-5C, increased CD206 and NOS2 expression was observed in the subcapsular and cortex zone of metastatic LNs of exosomes-injected mice compared with PBS-injected mice. The macrophages in metastatic LNs exhibited mixed phenotypes, expressing both CD206 and NOS2. The CD206-positive areas in exosome-injected LNs and PBS-injected LNs were 9.90% ± 0.83% and 2.41% ± 0.38% (P = 0.0002), respectively (Figure 1-5D). The NOS2-positive areas in exosome-injected LNs and PBS-injected LNs were 7.35% ± 0.58% and 2.15% ± 0.33% (P = 0.0002), respectively (Figure 1-5D). The ratio of M2 (CD206)

to M1 (NOS2) macrophages increased by approximately 1.5-fold in exosome-injected LNs compared with PBS-injected LNs. This finding indicates that crosstalk between TNBC cell-derived exosomes and M2 polarized macrophages was more extensive in promoting axillary LN metastasis.

DISCUSSION

We demonstrate that aggressive TNBC cell (MDA-MB-231)-derived exosomes function as intracellular links between cancer cells and macrophages. We demonstrated that TNBC cell-derived exosomes are a factor in (upregulation of CD206 and Arginase-1) to the benefit of breast cancer cells in vitro and *in vivo*, supporting enhanced tumor growth and axillary LN metastasis in an orthotopic TNBC model. We observed increases in primary tumor growth and axillary LN metastasis in orthotopic TNBC mice intravenously administered TNBC cell-derived exosomes using noninvasive BLI and US-guided PAI. Our results provide the evidence of an activator of TNBC cell-derived exosomes capable of accelerating tumor progression and LN metastatic dissemination in TNBC. Our findings are consistent with research that determined exosomes secreted from the other types of tumor cells, including pancreatic, ovarian, and gastric cancer cells, appear to promote metastasis [17-22].

Noninvasive imaging of exosomes expressing reporter proteins enables real-time tracking of intracellular transfer of exosomes. We established a TNBC cell line (MDA-MB-231/CD63-RFP cells) that

produces RFP-tagged exosomes by introduction of CD63-RFP fusion genes to enable the noninvasive monitoring of exosome transfer between TNBC cells and macrophages (RAW264.7). Co-culture or exosome administration enabled noninvasive monitoring of the intracellular transfer of RFP-tagged exosomes between cancer cells and macrophages, which demonstrated that TNBC cell-derived exosome transfer is dynamic. We visualized the exosomes from cells that harbor the Glu-lactadherin construct, a reporter protein that emits bioluminescence, in vivo after intravenous injection [26]. Noninvasive imaging tools for direct exosome tracking by optical reporter can be used to explore the pathophysiological function of exosomes in organs during tumor progression.

We investigated anti-EGFR-enhanced signal analysis of PAI in each axillary LN of PBS-injected or exosome-injected mice. PAI integrates with the clinical US imaging system, US-guided PAI, to simultaneously provide structural, functional, and molecular information at clinically relevant penetration depths by use of exogenous contrast agents. This technique was introduced as an approach for more sensitive and accurate detection of tumor and LN metastases in vivo [27-29]. We previously reported that anti-

EGFR-GNs-enhanced PAI is more sensitive than bioluminescence imaging for the detection of axillary LN micrometastasis [25]. The accuracy of PAI-detected LN metastasis was significant in 75% of mice (6 of 8 mice) based on correlation with histological analysis. In the present study, PAI detects axillary LN metastasis only when the area exhibits more than 3% EGFR immunostaining. Although these imaging approaches have demonstrated potential in providing useful morphological and functional information to detect LN metastasis, an imaging technique that can accurately detect LN micrometastases in real-time is needed.

Cancer cells communicate with neighboring cells via exosomes or other pathways to induce primary tumor growth and metastatic outgrowth. Macrophages exhibited plasticity via the M1 to M2 switch at various steps to enhance tumor initiation, growth, and metastasis. The presence of M2-type macrophages is clinically associated with poor prognosis in various types of cancers [30], which suggests that macrophages induce metastatic development by distinct cellular interactions within metastatic sites. Compared with ER-positive breast cancer cells, aggressive TNBC cells exert macrophage immunomodulation and induce M2-like polarization and inflammatory

cytokine production [16, 17]. Increased numbers of M2-type macrophages are found in metastatic LNs and are considered an index to predict LN metastasis [14, 15, 31]. Consistent with the aforementioned studies, we observed TNBC-derived exosome-induced macrophage programming and upregulation of both M1 marker (NOS2) and M2 marker (CD206, Arginase-1) in cultured macrophages taking up RFP-tagged exosomes and metastatic LNs of mice injected with RFP-tagged exosomes. After exosome administration, NOS2 expression was detected in the axillary LNs of tumor-bearing mice but not in the axillary of healthy mice without tumors, and upregulated in the metastatic LNs. Such differences might be caused by the number of cancer-derived exosomes required to induce NOS2 expression. Thus, the exosomes continuously released from metastatic LNs and additional exosome administration are enough to induce NOS2 expression in tumor-bearing mice. Our finding is consistent with a previous study that reports the association with high NOS2 expression and metastasis in breast cancer patients [32]. Metastatic TNBC cells assessed by EGFR, CK8/18/19, or GFP immunostaining were localized in the cortex zones of the axillary LNs. Many CD206-positive M2-type

macrophages were also localized in the cortex zone of axillary LNs in RFP-tagged exosome-injected mice. These results suggest that the increase in M2-type macrophages promotes LN metastasis and might be an attractive index for LN metastasis in TNBC patients.

Cancer exosomes are carriers of pro-tumorigenic molecules, such as protein, mRNA, microRNAs, and lipids, that induce macrophage polarization, thereby promoting cancer growth and metastasis [33]. Studies have revealed the exosomal molecules associated with macrophage immunomodulation in diverse cancers. Exosomes derived from ovarian cancer deliver microRNA-940 to induce macrophage M2 polarization [20]. Milk fat globule-EGF factor 8 (MGF-E8) upregulation in exosome proteins isolated from patients with primary and metastatic prostate cancer is associated with M2-type macrophage polarization [34]. miR-155 and miR-125b-2 transduction in pancreatic cancer cell (Panc-1)-derived exosomes converts the M2 phenotype back to the M1 phenotype [18]. Exosomal annexin II derived from breast cancer cells (MDA-MB-231) promotes breast cancer metastasis through macrophage-induced angiogenesis [35]. Wnt5a enrichment in breast cancer cell (SKBR-3)-derived exosomes is associated with macrophage-

induced invasion of breast cancer cells [36]. Ovarian cancer cell (SKOV-3)-derived exosomal miR-222 induces polarization of M2-type macrophages for tumor promotion [22]. miR-19a-3p downregulation induced by conditioned medium of breast cancer cells (4T1) is associated with M2-type macrophage polarization, resulting in breast cancer progression and metastasis [37].

Our study demonstrates that TNBC-derived exosomes are a factor in tumor growth and LN metastasis through intercellular communication with macrophages. However, the crucial contents of breast cancer exosomes are still not fully elucidated, and considerable research is needed to understand the role of TNBC cell-derived exosomes in macrophage polarization and breast cancer progression. Our next study will focus on identifying the crucial molecular components of TNBC cell-derived exosomes and deciphering the molecular mechanisms involved in macrophage polarization and LN metastasis.

Chapter 2

Noninvasive Photoacoustic Imaging of Dendritic Cell Stimulated with Breast Cancer Cell–Derived Exosomes

INTRODUCTION

Dendritic cells (DCs) are the most potent antigen-presenting cells of the immune system due to their notable ability to induce T cell-mediated antitumor effects [38]. Although DCs have been used in the treatment of diverse cancers, including melanoma, prostate cancer, malignant glioma, and renal cell carcinoma [39-41], the current methods of DC activation and maturation through antigen loading with peptides, cytokines, and cell lysates have led to unsatisfactory outcomes, both in preclinical and clinical cancer immunotherapy [42]. To improve the efficacy of DC-based immunotherapy, the optimal method for efficient DC activation and maturation and tumor-antigen loading into DCs is still required.

Exosomes are extracellular vesicles of 30-100 nm in diameter that carry many contents of cells, including miRNAs, proteins, lipids, and even DNAs, and they are emerging as an important mediator of intracellular communication by transferring functional effectors to neighboring cells [43]. Tumor cell-derived exosomes contain tumor-specific antigens, such as melan-A, gp-100 proteins, mesothelin, and human epidermal growth factor receptor 2 [44-47].

The activation and maturation of DCs are assessed by the expression of the costimulatory molecules CD40, CD80 and CD86, which are required for T cell activation, and the CC-chemokine receptor 7 (CCR7), which leads to the migration of DCs from tissues to draining lymph nodes (LNs) [48]. Exosome-stimulated DCs display higher expression levels of CD40, CD80, and CD86 than tumor lysate-stimulated DCs [42, 46, 49]. These studies suggest that breast cancer cell-derived exosomes might be a relevant carrier to efficiently deliver tumor-specific antigens to DCs and elicit DC-mediated anti-tumor immunity.

For successful DC-based immunotherapy, the sufficient migration of viable DCs from the primary administration site into LNs is crucial for T cell activation [50]. Noninvasive imaging of DCs labeled with a biocompatible contrast agent can provide important information regarding the migration route and persistence of the injected DCs in targeted LNs in vivo, help improve the efficiency of DC-based immunotherapy, and predict the outcomes of DC-based immunotherapy. Photoacoustic imaging (PAI) is currently one of the fastest-growing molecular imaging tools that combines the high contrast of optical imaging with the high spatial resolution of

ultrasound (US) [51, 52]. More importantly, because of the ease of use, lack of ionizing radiation and relatively low cost of PAI when compared to traditional radiologic methods, such as magnetic resonance imaging (MRI), positron emission tomography (PET) or computed tomography (CT), PAI has rapidly been adopted in preclinical and clinical practices as a promising alternative to traditional imaging tools [53]. Gold nanoparticles (GNs) have been proposed as a good contrast agent for PAI due to partially fulfilling basic requirements for cell labeling strategies, i.e., long-term stability, low cytotoxicity, and no interference with biological function [25, 52-54]. GNs have entered preclinical and clinical studies as imaging agents as well carriers due to their ease of functionalization with antigens, adjuvants, and targeting molecules [55-57]. Thus, GN-labeled DCs could be easily and longitudinally tracked using PAI, but there is still a lack of reliable and robust evidence of PAI for tracking GN-labeled DCs in vivo.

In this study, we therefore investigated whether exosome derived from breast cancer cells can be used as a potent source to activate DCs and whether US-guided PAI allows for sensitive tracking of exosome-stimulated DC migration toward LNs in vivo using GNs.

MATERIALS AND METHODS

Cell culture and reagents

The murine mammary carcinoma 4T1, which produces highly metastatic and poorly *immunogenic* breast cancer cell line in BALB/c mice [58], was obtained from the Lee Gil Ya Cancer and Diabetes Institute (Incheon, Korea). DC2.4, which is immortalized murine DCs created by transducing bone marrow isolates of C57BL/6 mice with retrovirus vectors expressing murine GM-CSF and the myc and raf oncogenes [59], was kindly provided by K. L. Rock in Dana-Farber Cancer Institute (Boston, MA, USA). The 4T1 cells were cultured in DMEM (WelGENE, Daegu, Korea) containing 10% fetal bovine serum and 1% penicillin/streptomycin. DC2.4 cells were cultured in RPMI 1640 medium (WelGENE) supplemented with 10% fetal bovine serum, 1% penicillin-streptomycin-glutamine, 1% nonessential amino acids, 1% HEPES buffer and 55 μM 2-mercaptoethanol in a 5% CO2 incubator at 37° C. When the DC2.4 cells are approximately 80-85% confluent, the subculture was performed. In order not to significantly affect the cell marker expression and functionality, DC2.4 cells were cultured for at least 10 passages after initial

thawing.

Stable cell line establishment and confocal microscopy analysis

A stable 4T1 cell line overexpressing the exosomal CD63- RFP fusion protein was generated by lentiviral transduction (pCT-CD63-RFP Cyto-Tracer) (System Biosciences, Palo Alto, CA, USA). A stable DC2.4 cell line expressing GFP protein was generated by lentiviral transduction. Then, GFP-positive DC2.4 cells and RFP-positive 4T1 cells were sorted using a FACSCalibur flow cytometer (BD Biosciences, Franklin Lakes, NJ, USA). A laser scanning confocal microscope (Leica, Wetzlar, Germany) was used for visualization of 4T1 cells expressing CD63-RFP and DC2.4 cells expressing GFP at 558 nm/605 nm and 488 nm/509 nm for excitation/emission, respectively.

Exosome isolation and nanosight analysis

Conditioned media were obtained from 4T1/CD63-RFP cells grown at subconfluence for 3 to 4 days in growth media containing serum depleted of bovine exosomes (Gibco Laboratories, Carlsbad, CA, USA). exosomes were isolated from collected conditioned media using the Exo-spin™ Exosome Purification Kit according to the

manufacturer’s instructions (Cell Guidance Systems, Cambridge, UK). Total protein concentration of exosomes was quantified by using the Pierce Micro-BCA Protein Assay Kit (ThermoScientific, Waltham, MA, USA). The size distribution and concentration of exosomes were determined using a NanoSight NS500 (Malvern, Grovewood road, UK) equipped with a 642 nm laser and CCD camera, and data were analyzed with the Nanoparticle Tracking Analysis (NTA) software (version 3.1 Build 3.1.54) as described [60]. In brief, the samples were diluted sufficiently for the contrast and minimal background level. The particle motion video was recorded automatically using standard measurement mode (temperature: 20.8–21.0 ° C and viscosity: 0.976–0.981 cP). The captured videos (five videos per sample) were processed and analyzed (camera level: 10, capture duration: 60 s, and detection threshold: 3). Purified exosomes were then stored at − 80 ° C until use.

Imaging of exosome transfer in cultured DCs

For live imaging of TEX uptake by DC2.4 cells, GFP-transduced DC2.4 cells (1×10^4) were seeded in Nunc™ Glass Bottom Dish and allowed to attach in exosome-depleted FBS media. At 24 h, 48

h, and 72 h after administration of 10 μg of exosomes s into GFP-transduced DC2.4 cells, the cellular uptake of exosomes was monitored by using a laser scanning confocal microscope (Leica).

Real-Time RT-PCR

DC2.4 cells were stimulated with exosomes (10 μg/ml) for 72 h or LPS (100 ng/ml) for 12 h. After extraction of total RNA from cultured cells using TRIzol reagent (Invitrogen, Carlsbad, CA, USA), cDNA was produced using Super-Script II reverse transcriptase (Invitrogen). Real-time PCRs were run on an ABI 7500 system utilizing a SYBR Green PCR master mix (Applied Biosystems, Foster City, CA, USA) and specific primers for TNF-α (forward: 5′ GCCTCTTCTCATTCCTGCTTG3′ and reverse: 5′ CTGATGAGAGGGAGGCCATT3′) and β-actin (forward: 5′ TTCCTGGGCATGGAGTCCTG3′ and reverse: 5′ CGCCTAGAAGCATTTGCGGT3′). The results were analyzed by the $2^{-\Delta\Delta CT}$ method [61], which reflects the threshold difference between a target gene and β-actin in each sample and the relative gene expression set to 1 for unstimulated DC2.4 cells (PBS samples).

Western blot analysis

4T1 cells and DC2.4 cells were lysed in RIPA buffer (Sigma-Aldrich, St. Louis, MO, USA). The proteins extracted from 4T1 cells, DC2.4 cells, and purified exosomes s were separated using SDS-PAGE and were transferred to nitrocellulose membranes. The membranes were blocked using 5 % skim milk in Tris-buffered saline containing 0.05 % Tween-20 and were incubated overnight at 4 ° C with primary antibodies directed against RFP (Abcam, Cambridge, MA, USA), CCR7 (Abcam), CD63 (Santa Cruz Biotechnology, Dallas, Texas, USA), Alix (Santa Cruz Biotechnology), Calnexin (Sigma-Aldrich), and β-actin (Sigma-Aldrich) and then incubated with HRP-conjugated secondary antibodies (Santa Cruz Biotechnology). The blotted membranes were visualized using enhanced chemi-luminescence reagents (GE Healthcare, Danderyd, Sweden). Quantification of band intensities on the Western blot was carried out using ImageJ software provided by NIH Image and normalized to levels of β actin.

Proliferation assay

DC2.4 cells (5×10^3) were seeded in a 48-well plate and incubated in exosome-depleted FBS media for 24 h. exosomes (5-10 μg/ml)

were administered to DC2.4 cells for 24–72 h. Briefly, 3-(4,5-dimethylthiazol-2-yl)-2,5-diphenyltetrazolium bromide (MTT) reagent (250 μg/ml) was added to each well and incubated for 1 h at 37 ° C. Formazan crystals were solubilized by the addition of 150 μl of dimethyl sulfoxide to each well. The optical density (OD) at 540 nm was measured by using a microplate reader (GE Healthcare), and the cell proliferation rate was determined.

Transwell migration assay

DC2.4 cells (1×10^5) were activated with exosomes (10 μg/ml) or a complex with TNF-α (20 ng/ml) and IFN-γ (20 ng/ml), which were deposited in the upper chamber of the transwell plate with a 0.8-μm pore size (Corning, Lowell, MA USA). The lower chamber was filled with 500 μl of serum-free medium with CC-chemokine ligand 19 (CCL19, 250 ng/ml) and CCL21 (250 ng/ml). Cells that migrated into the lower chamber for 24 h were fixed in 4 % paraformaldehyde and stained with crystal violet, and the stained images were captured by light microscopy. Crystal violet from the stained membrane was finally extracted with 1 % sodium dodecyl sulfate. The optical density (OD) at 550 nm was measured by using

a microplate reader (GE Healthcare), and cell migration was determined.

Flow cytometry

The expression of CD40, CD80, and CD86 on DC2.4 cells was analyzed using flow cytometry. DC2.4 cells were collected and washed twice with ice-cold PBS containing 1 % BSA. Cells were incubated with anti-CD40-FITC, anti- CD80-FITC, and anti-CD86-FITC antibodies (all from BD Biosciences, Franklin Lakes, NJ) for 30 min at 4 ° C. Cell-associated fluorescence was measured using a FACSCalibur (BD Biosciences). Data were analyzed by CELLQuest v3.3 (BD Biosciences).

GN preparation and cell labeling

Rod-shaped GNs (10 nm × 40 nm) with surface plasmon resonance at 808 nm were purchased from Nanopartz Inc. (Lovel, CO, USA). In brief, highly stable 10 × 41-nm cetyltrimethylammonium bromide (CTAB)-coated GNs with longitudinal plasmon resonance at 808 nm were synthesized using a proprietary seed growth method. An SH-terminated branched amine polymer manufactured by Nanopartz was used to replace the CTAB. Centrifugation and dialysis against sterile

phosphate-buffered saline were used in all steps of binding and purification. Loading of antibodies was determined using a proprietary method incorporating HPLC and UV-Vis. Further sterilization and endotoxin testing were performed. DC2.4 cells were incubated with GNs (60 -240 pmol/l) for 12-24 h at 37 ° C and 5 % CO2 and washed four times with PBS to remove unbound GNs.

Animal and injection of exosome-stimulated and GN-labeled DCs

All animal experiments were approved by the Seoul National University Hospital Biomedical Research Institute Animal Care and Use Committee (IACUC No. 16-0102- C2A0). Five- to six-week-old C57BL/6 male mice (n = 10) were subcutaneously preinjected 24 h earlier with TNF-α (40 ng, Sigma-Aldrich). DC2.4 cells were treated with exosomes (10 μg/ml) or PBS for 60 h and then were labeled or unlabeled with GN (120 pmol/l) for 12 h. In order to examine the feasibility of US-guided PAI for ex vivo LN injected with GN-labeled DC2.4 cells, a total of 3×10^6 GN-labeled DC2.4 cells (DC-GN) were directly injected into the axillary LNs of mice (n = 3) and axillary LNs removed from mice right away. For tracking the *in vivo* migration of GN-labeled DC2.4 cells into axillary LNs, ten

mice were randomly assigned to each of two experimental groups as follows: exosomes −stimulated and GN−labeled DC2.4 cell injected mice (DC + exosomes +GN: n = 5) vs only GN−labeled DC2.4 cell−injected mice (DC + GN: n = 5). After a total of 3×10^7 DC2.4 cells in 30− μl PBS was injected subcutaneously into the foreleg footpads, DC2.4 cells that migrated into axillary LNs were longitudinally monitored by US−guided PAI *in vivo* at 4 h and 24 h and analyzed by silver staining and immunohistochemistry for GFP.

US−guided PAI

The Vevo2100 LAZR imaging system (FUJIFILM VisualSonics Inc., Toronto, Ontario, Canada) equipped with a LZ−550 integrated fiberoptics transducer (256 sensitive piezoelectric elements for acoustic detection, broadband frequency: 32–55 MHz, image width: 14 mm, image depth: 15 mm, image axial and lateral resolution: 45 μm and 90 μm) and a pulsed laser (OPOTEK Inc., Carlsbad, CA, tunable in 2−nm increments from 680 to 970 nm, 20 Hz repetition rate, 5 ns pulse width, 50 mJ pulse energy) was used to acquire all PA and US images.

For acquiring in vitro US−guided PA images and PA signals, a

compacted pellet of GN-labeled or unlabeled DC2.4 cells (5×10^5, 1×10^6, 2×10^6, and 1×10^7) fixed with 4 % paraformaldehyde was formed at the bottom of a 0.2-ml sterile PCR tube by centrifugation, and the remaining tube volume was filled with PBS. A control was made with an equivalent number of unlabeled DC2.4 cells. Ultrasound gel was centrifuged (to remove air bubbles) and applied to directly couple the transducer to the surface of PCR tubes placed on ultrasound gel pad. For the analysis of ex vivo US-guided PA images and signals, axillary LNs were immediately removed from mice after the injection of GN-labeled DC2.4 cells into axillary LNs and fixed with 10 % formalin solution. Ultrasound gel was applied to directly couple the transducer to the fixed axillary LNs placed on ultrasound gel pad. For the analysis of *in vivo* US-guided PA images and signals, warmed ultrasound gel (37 ° C) was applied to directly couple the transducer to the surface of axillary LN region of mice before and at 4 h and 24 h after the injection of GN-labeled DC2.4 cells into footpad.

To collect anatomical information at high resolution, B-mode imaging was acquired using a high-frequency ultrasound probe. On PA mode, the laser was tuned to optical wavelengths from 680 to 850

nm, with a frequency of 40 MHz, PA power of 100 %, and a PA signal gain of 40 dB. PA images were averaged eight times, thus suppressing uncorrelated noise. Images and PA signals coming from GNs in cell pellets and ex vivo and *in vivo* axillary LNs were determined by using Unmixing program (Vevo® Spectro software (FUJIFILM VisualSonics Inc) to select imaging wavelengths for spectroscopic photoacoustics given the spectra of expected chromophores [62]. A region of interest (ROI) around the cell pellets and LNs was drawn on image slices, as identified on the digitally stored US images. The absorption spectrum coming from GNs was displayed. The PA image was displayed on a color scale and superimposed on the corresponding gray-scale US image. The spectrally unmixed PA signals in the ROIs drawn on images of cell pellets and axillary LNs were measured. The highest PA signal coming from GNs in cell pellets and ex vivo and *in vivo* axillary LNs was detected at 770- 800 nm. The unit for PA signal measurement is an arbitrary unit (AU).

Histological analysis

Axillary LNs were removed 24 h after the injection of DC2.4 cells,

fixed with 4 % buffered formalin, and embedded in paraffin blocks. Tissues were sectioned into 4-μm-thick sections. Hematoxylin and eosin (H&E) staining for analyzing the cell death as well as the histological structure were performed. Silver staining for detecting GN-labeled DCs was performed using Silver Enhancer Kit (Sigma-Aldrich). Immunostaining was performed with antibodies against GFP (Abcam) and an appropriate secondary antibody and was subsequently stained with counter hematoxylin solution (Millipore Ltd., Darmstadt, Germany). Histological images of stained tissues were acquired using a microscope (Leica) equipped with a CCD camera (Leica).

Statistical analyses

All experiments were performed in three or five independent samples for each condition and repeated at least three times. The results are expressed as the mean ± standard error (S.E.). The statistical comparisons between two independent groups were made using the two-tailed unpaired t test, whereas analysis of variance (ANOVA) was performed on multiple comparisons of groups. A P value less than 0.05 was considered statistically significant. Statistical analyses

were performed by GraphPad Prism 5.0 (GraphPad Software, Inc., La Jolla, CA, USA).

RESULTS

Analysis of exosomes derived from breast cancer cells expressing the exosome marker CD63-RFP

We established a 4T1 cell line that stably expresses a common exosomal marker of CD63 tagged with RFP. Confocal fluorescence images revealed RFP-tagged exosomes produced from 4T1 cells (Figure 2-1A). From NanoSight analysis, exosomes released from 4T1 cells exhibited heterogeneous sizes ranging from 100 to 200 nm in diameter (Figure 2-1B). Western blot revealed that purified exosome expressed specific exosomal marker proteins, such as CD63 and Alix, but not the endoplasmic reticulum membrane marker Calnexin (Figure 2-1C).

Proliferation activity and properties of exosome-stimulated DCs

To investigate whether exosomes play a role in the proliferation activity of DC2.4 cells, an MTT assay was performed after different amounts of exosomes (5 and 10 μg/ml) were supplied to DC2.4 cells for 24-72 h. The addition of exosomes (5-10 μg/ml) promoted the proliferation activity of dose- or time-dependent DC2.4 cells (Figure 2-2A). To visualize the exosome uptake by DC2.4 cells, live

cell imaging was performed using confocal laser scanning microscopy. DC2.4 cells largely had a round shape with an adherent behavior and formed small clusters, but DC2.4 cells matured with LPS (100 ng/ml) exhibited prominent spindle-shaped morphology (data not shown). Interestingly, when RFP-tagged exosomes (10 μg/ml) were translocated into GFP-transduced DC2.4 cells, spindle-shaped morphological changes were observed in exosome-stimulated DC2.4 cells at 72 h (Figure 2-2B). DCs matured in the presence of LPS were characterized by the enhanced expression of costimulatory molecules, e.g., CD40, CD80, and CD86, which are important for effective T cell activation. The expression levels of costimulatory molecules on the surface of exosome-stimulated DC2.4 cells were analyzed by flow cytometry. The administration of exosomes (10 μg/ml) significantly increased the levels of CD40 (29.70 $\pm$ 5.64, P = 0.0001), CD80 (48.12 $\pm$ 2.99, P = 0.0021), but there was no significant in the level of CD86 (79.98 $\pm$ 9.38, P = 0.9452) (Figure 2-2C). Similar to LPS stimulation, exosomes (10 μg/ml) elicited a significant upregulation of TNF-α, which is a well-known maturation and survival factor for DCs (6.49 $\pm$ 0.16, P < 0.0001) (Figure 2-2D). CCR7 is a crucial receptor involved in DC function *in*

vivo because it governs cell migration to LNs. Exosomes (10 μg/ml) induced a 1.5-fold increase in CCR7 protein levels (1.5 $\pm$ 1.68, P = 0.0126) compared with the stimulation by TNF-α and IFN-γ (20 ng/ml) (Figure 2-2E).

Cytotoxicity and in vitro US-guided PAI of GN-labeled DCs

To determine the optimal conditions for labeling with GNs, different amounts of GNs (60-240 pM) were supplied to the cultures of DC2.4 cells, and the MTT assay was assessed. A 12-h incubation of GNs at 60-240 pM did not cause cytotoxicity, but a 24-h incubation of GNs elicited dose-dependent cytotoxicity (Figure 2-3A). In DC2.4 cells labeled with GN (120 pM) for 12 h, a significant alteration in the expression levels of CD40, CD86, and CCR7 was not observed (data not shown). Therefore, the optimal DC labeling conditions were determined at 120 pM and for 12 h.

Silver staining revealed intracellular localization of GNs (dark gray spots) taken up by DC2.4 cells as well as exosome-stimulated DC2.4 cells (Figure 2-3B left). To examine whether GN labeling interferes with the migratory ability of exosome-stimulated DC2.4 cells, transwell migration and crystal violet assays were performed. The

migratory ability of DC2.4 cells toward the chemokines (CCL19 and CCL21) was significantly higher in the exosome-treated group (0.24 ± 0.01, P < 0.0001) than in the TNF-α plus IFN-γ-treated group (0.10 ± 0.01) (Figure 2-3C). Photos of Figure 2-3D showed US-guided PA images and US images of GN-labeled DC2.4 cell pellets at different cell numbers. PAI signals were quantified from cells collected after 12-h incubation with 120 pM. The PA signal values of 5×10^5, 1×10^6, 2×10^6, and 1×10^7 GN-labeled exosome-DC2.4 cells were 0.17 ± 0.01 (P = 0.0123), 0.61 ± 0.05 (P = 0.0004), 0.90 ± 0.04 (P < 0.0001), and 1.16 ± 0.03 (P < 0.0001), respectively, thus showing that the amplitude of PA signals was proportional to the cell number (Figure 2-3D).

US-guided PAI of GN-labeled and exosome-stimulated DC migration into LNs

We investigated the feasibility of US-guided PAI for noninvasively detecting GN-labeled DC2.4 cells after direct injection of DC2.4 cells into axillary LNs. A strong PA signal can be detected in DC + GN-injected LNs (0.73 ± 0.15) compared with noninjected LNs (0.16 ± 0.01) (P = 0.024) (Figure 2-4A), GFP immunostaining and silver staining showed the existence of GFP and GNs in DC2.4 cells injected

into LNs (Figure 2-4B).

We next explored whether exosomes promote DC2.4 cell migratory ability in vivo and whether GN labeling allows for the noninvasive detection of exosome -stimulated DC2.4 cell migration into draining popliteal LNs using PAI. For the *in vivo* study, we used GFP-transduced DC2.4 cells. *In vivo* US-guided PAI of axillary LNs were acquired before and 4- 24 h after the injection of GN-labeled DC2.4 cells (DC + GN) and GN-labeled and exosome-stimulated DC2.4 cells (DC + exosome + GN) into the footpad of mice. The mean PA signal of axillary LNs before the injection of DC2.4 cells was 0.22 ± 7.0. The pre- and post-US-guided PAI showed an increase in GN-enhanced PA signals on the axillary LNs of DC + exosome + GN mice at 24 h post-injection, while DC + GN mice did not lead to such signal changes (Figure 2-4C left). At 24 h post-injection, the mean PA signals of the axillary LNs in DC + exosome + GN mice significantly increased compared to those of DC + GN mice (0.19 ± 0.04 versus 0.38 ± 0.07, P = 0.048) (Figure 2-4C right).

We carried out histological analysis for the correlation with PAI of

the axillary LNs in the DC + GN and DC + exosome + GN mice at 24 h after the injection of DC2.4 cells. H&E staining showed no structural differences or cytotoxicity in the LNs of DC + GN and DC + exosome + GN mice. GFP immunostaining and silver staining of microsections clearly revealed that exosomes elicited DC2.4 cell migration into the cortex of LNs (Figure 2−4D) which correlated well with an increase in the PA signal value of axillary LNs of DC + exosome + GN mice.

DISCUSSION

In the present study, we have showed that exosomes induce DC activation and maturation without cytotoxicity, suggesting the possibility to use the DCs stimulated with exosomes in DC-based immunotherapy. We have shown that GN can be used for direct DC labeling without hampering the important biological functions of DCs, e.g., low cytotoxicity and no interference in migration ability, and costimulatory molecule expression. Moreover, US-guided PAI using direct labeling with GNs can be readily accessible and easy for noninvasive tracking and monitoring of exosome-stimulated DC migration into LNs.

Exosome can mediate pro-tumor or anti-tumor immune responses by activating or impairing the functions of immune cells such as macrophages, T cells, and DCs [63-67]. Exosomes can be utilized as efficient antigen carriers compared with traditional tumor lysates because exosomes have tumor cell-specific antigens as well as many important immunological molecules [44, 49]. In this study, 5-10 μg/ml of exosomes (exosomes secreted from mouse breast cancer cells 4T1) easily taken up by DCs (bone marrow-derived DC

cells, DC2.4), increased DC proliferation and migration abilities and upregulated cytokine TNFα associated with DC maturation and survival [68] and CCR7 involved in DC migration [69]. We provided clear evidence that, similar to LPS-stimulated DCs, exosomes induced the upregulation of costimulatory molecules CD40, CD80, and CD86 on DCs for more effective T cell priming. Contrary to our results, at 50-100 μg/ml, exosomes isolated from breast cancer cells (4T1, MDA-MB-231), melanoma (B16) or lung cancer cells (LLC) upregulate PD-L1 and suppress CCR7, CD80 and CD86 expression on DCs, resulting in inducing apoptosis and blocking DC maturation and migration [65, 66], indicating that a higher dose of exosomes ($\geq$50 μg/ml) can cause immunosuppressive effects. In the case of exosomes derived from myeloid leukemia cell (WEHI3B), even at a concentration of 50-100 μg, exosomes do not display an immunosuppressive impact on DCs, and the survival time of mice was more efficiently prolonged when mice treated with DCs stimulated with exosomes were vaccinated with tumor lysates [70], implying that the effect of exosomes on cancer immunomodulation might be dependent on their origin. Based on our results, the concentration of

exosomes originating from breast cancer cells 4T1 was less than ≤ 10 μg/ml for the application of ex vivo exosome-stimulated DC immunotherapy.

Monitoring the in vivo distribution and migration of DCs is critical for tailoring and optimizing DC-based immunotherapy. Although scintigraphy [71, 72], PET [73-75], MRI [76, 77], and optical imaging [78-80] has been applied for DC imaging, the development of imaging method for cost-efficient, convenient, sensitive and real-time detection of DCs in vivo still remains challenging. PAI can be easily combined with US and has been readily accepted by clinicians in recent decades for biomedical imaging due to the hybrid merit of optical absorption and ultrasound detection, relative inexpensiveness, ease of use, and real-time imaging technology [52, 53]. GNs have been widely used as excellent contrast agents of PAI and have major advantages, including a low toxicity profile, and the Food and Drug Administration approval for clinical pilot studies [55, 57]; nevertheless, there are no trials for noninvasive monitoring of GN-labeled DC migration into LNs with US-guided PAI. Rod-shaped GNs (40 ×10 nm) that we used in this study were easily taken up by

DC2.4 cells and had no notable cytotoxicity after a 12 h incubation at 120–240 pM, but a 24 h incubation at 60–240 pM resulted in decreased DC2.4 cell proliferation. Moreover, we have demonstrated that GN–labeled and exosome–stimulated DC2.4 cell migration into LNs can be monitored in real time through in vivo US–guided PAI, providing a generally applicable and cost–effective approach to predict and tailor DC–based immunotherapy for individualized immunological cancer treatments.

FIGURES

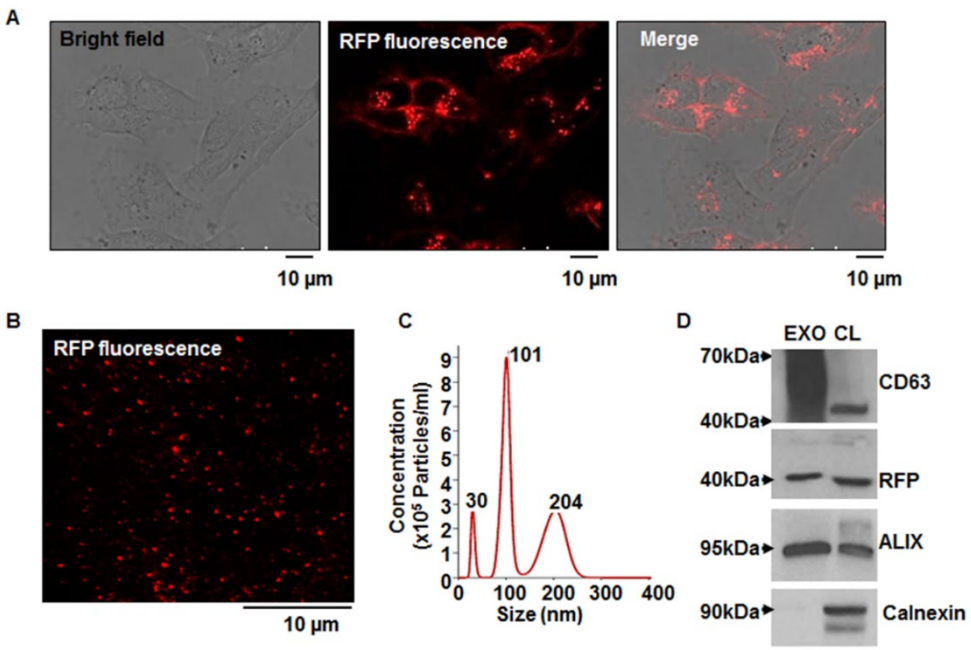

Figure 1-1. Generation of stable MDA-MB-231 cells overexpressing the exosomal CD63-RFP fusion protein and analysis of purified RFP-tagged exosomes. (A) Confocal images of CD63-RFP-transduced MDA-MB-231 cells. (B) Confocal image of purified RFP-tagged exosomes. (C) NanoSight analysis of the size and concentration of purified RFP-tagged exosomes. (D) Western blot of CD63, Alix, Calnexin, and RFP in the purified RFP-tagged exosome (EXO) and the lysates of MDA-MB-231/CD63-RFP cells (CL).

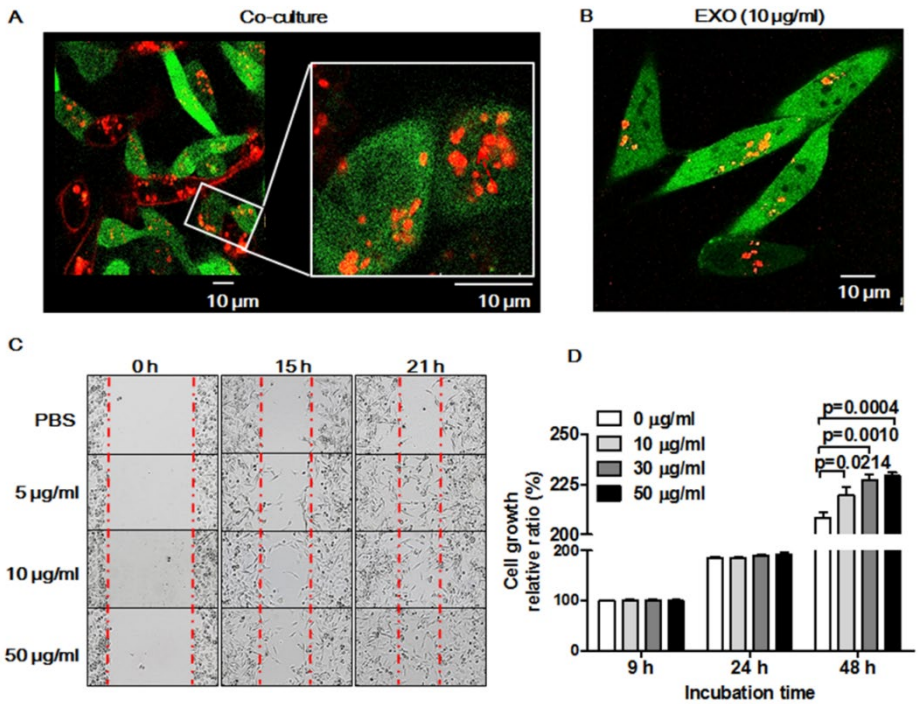

Figure 1-2. TNBC cell migration and proliferation is enhanced by TNBC cell-derived exosomes. (A) Confocal images of transportation of RFP-tagged exosomes in direct co-culture with MDA-MB-231/CD63-RFP cells and MDA-MB-231/GFP cells for 24 hours. (B) Confocal image of RFP-exosomes (EXO) taken up by MDA-MB-231/GFP cells after administration of RFP-tagged exosomes for 24 hours. (C) Wound-healing assay in MDA-MB-231 cells treated with RFP-tagged exosomes or PBS for 15 to 21 hours. (D) Proliferation assay of MDA-MB-231 cells treated with RFP-tagged exosomes or PBS for 24 to 48 hours.

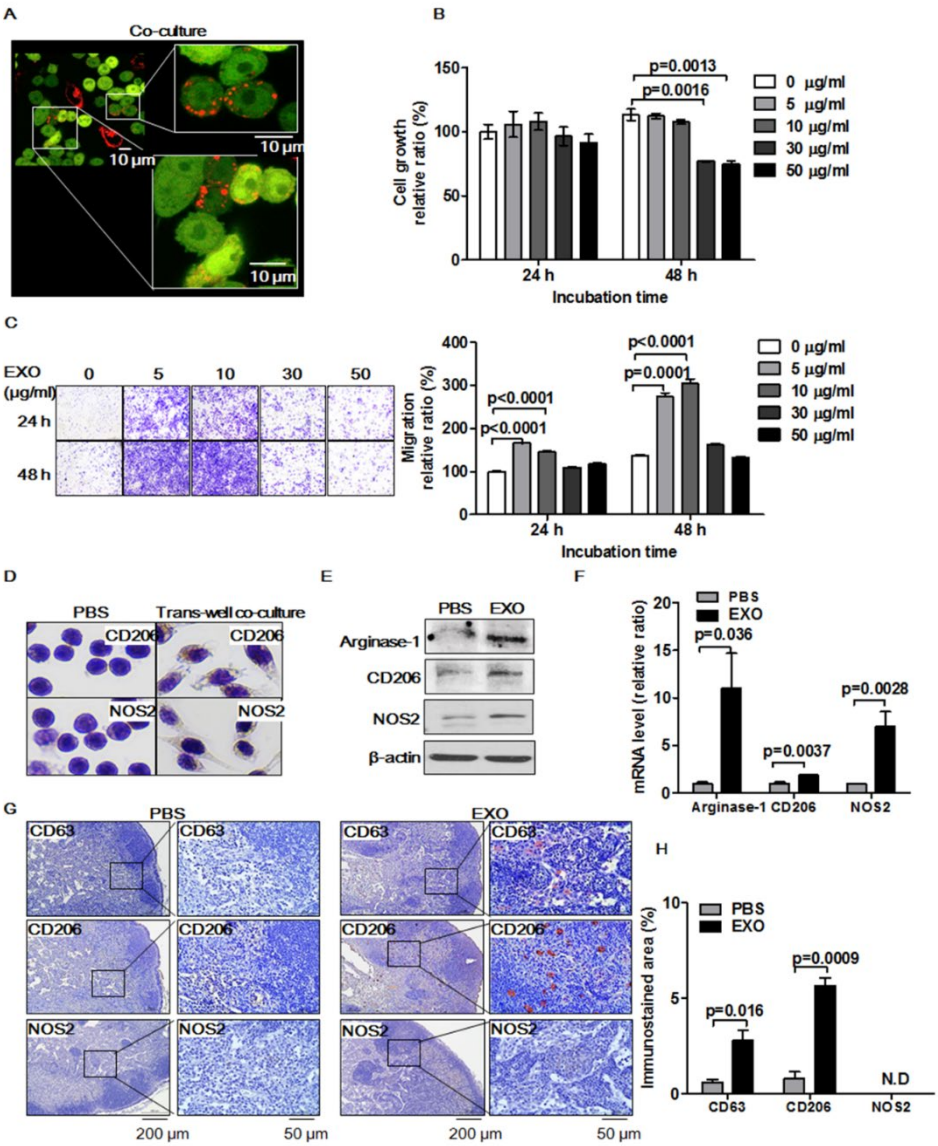
A
Co-culture
10 μm
10 μm
10 μm
B
Cell growth relative ratio (%)
150
100
50
0
p=0.0013
p=0.0016
0 μg/ml
5 μg/ml
10 μg/ml
30 μg/ml
50 μg/ml
24 h
48 h
Incubation time
C
EXO (μg/ml)
0
5
10
30
50
24 h
48 h
Migration relative ratio (%)
400
300
200
100
0
p<0.0001
p<0.0001
p<0.0001
p=0.0001
0 μg/ml
5 μg/ml
10 μg/ml
30 μg/ml
50 μg/ml
24 h
48 h
Incubation time
D
PBS
Trans-well co-culture
CD206
CD206
NOS2
NOS2
E
PBS
EXO
Arginase-1
CD206
NOS2
β-actin
F
PBS
EXO
mRNA level (relative ratio)
20
15
10
5
0
p=0.036
p=0.0037
p=0.0028
Arginase-1
CD206
NOS2
G
PBS
EXO
CD63
CD206
NOS2
200 μm
50 μm
200 μm
50 μm
H
Immunostained area (%)
10
5
0
PBS
EXO
p=0.016
p=0.0009
N.D
CD63
CD206
NOS2

Figure 1-3. Induction of M1/M2 polarization by TNBC cell-derived exosomes in vitro and *in vivo*. (A) Confocal images of RFP-tagged exosome transportation in direct co-culture with MDA-MB-231/CD63-RFP cells and RAW264.7/GFP cells for 24 hours. (B) Proliferation assay in RAW264.7 cells treated with RFP-tagged exosomes (30 or 50 μg/mL) or PBS for 24 to 48 hours. (C) Trans-well migration assay in RAW264.7 cells treated with RFP-tagged exosomes (EXO, 5-10 μg/mL) or PBS for 24 to 48 hours. (D) Immunostaining of CD206 and NOS2 in RAW264.7 cells cultivated with MDA-MB-231/CD63-RFP cells in the trans-well system for 24 hours. (E and F) Western blot and real-time RT-PCR of Arginase-1, CD206, and NOS2 in RAW264.7 cells administered RFP-tagged exosomes (10 μg/mL) or PBS for 24 to 48 hours. (G) Immunostaining images of CD63, CD206, and NOS2 in axillary LNs removed from mice at 3 hours after intravenous injection of RFP-tagged exosomes (100 μg) or PBS. (H) Quantitative immunostained area mean ± S.E.) of CD63, CD206, and NOS2. ND indicates no detection.

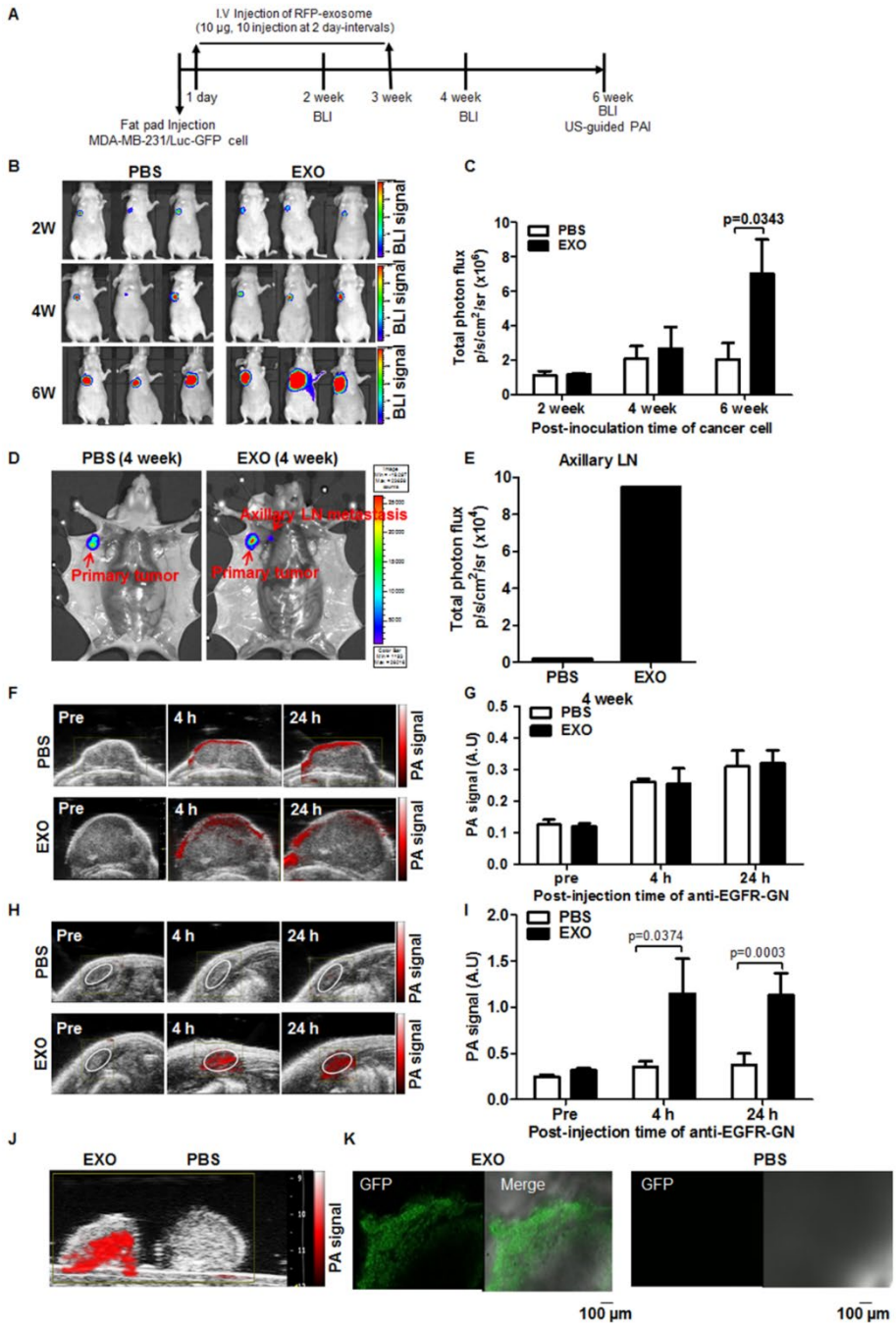
A
I.V Injection of RFP-exosome
(10 μg, 10 injection at 2 day-intervals)
1 day
2 week
3 week
4 week
6 week
Fat pad Injection
MDA-MB-231/Luc-GFP cell
BLI
BLI
BLI
US-guided PAI
B
PBS
EXO
2W
4W
6W
BLI signal
C
PBS
EXO
p=0.0343
Total photon flux p/s/cm²/sr (x10⁶)
2 week
4 week
6 week
Post-inoculation time of cancer cell
D
PBS (4 week)
EXO (4 week)
Axillary LN metastasis
Primary tumor
Primary tumor
E
Axillary LN
Total photon flux p/s/cm²/sr (x10⁴)
PBS
EXO
F
Pre
4 h
24 h
PBS
EXO
PA signal
G
4 week
PBS
EXO
PA signal (A.U)
pre
4 h
24 h
Post-injection time of anti-EGFR-GN
H
Pre
4 h
24 h
PBS
EXO
PA signal
I
PBS
EXO
p=0.0374
p=0.0003
PA signal (A.U)
Pre
4 h
24 h
Post-injection time of anti-EGFR-GN
J
EXO
PBS
PA signal
K
EXO
PBS
GFP
Merge
GFP
100 μm
100 μm

Figure 1-4. Noninvasive BLI and US-guided PAI of primary tumor growth and axillary LN metastasis promoted by cancer cell-derived exosomes in TNBC models. (A) A flowchart depicting the experimental design in an orthotropic tumor model. (B) Representative BLI of primary tumors of mice intravenously injected with PBS or RFP-tagged exosomes (EXO, 10 μg, 10 injections at 2 day-intervals) at 2, 4, and 6 weeks after fat pad injection with MDA-MB-231/Luc-GFP cells. (C) Total photon flux (mean ± S.E.) measured from primary tumors. (B and C) Representative BLI and total photon flux (mean ± S.E.) of axillary LN area in tumors from mice intravenously injected with PBS or exosomes at 4 weeks. (F and H) Representative US-guided PAI of primary tumor and axillary LNs of mice intravenously injected with PBS or RFP-tagged exosomes before and 4 hours and 24 hours after intratumor injection of anti-EGFR-GN (7.7 mg/kg). (G and I) PA signals (mean ± S.E.) measured from primary tumors and axillary LNs. (J and K) Representative ex vivo US-guided PAI and GFP confocal images of axillary LNs isolated from mice intravenously injected with PBS or RFP-tagged exosomes.

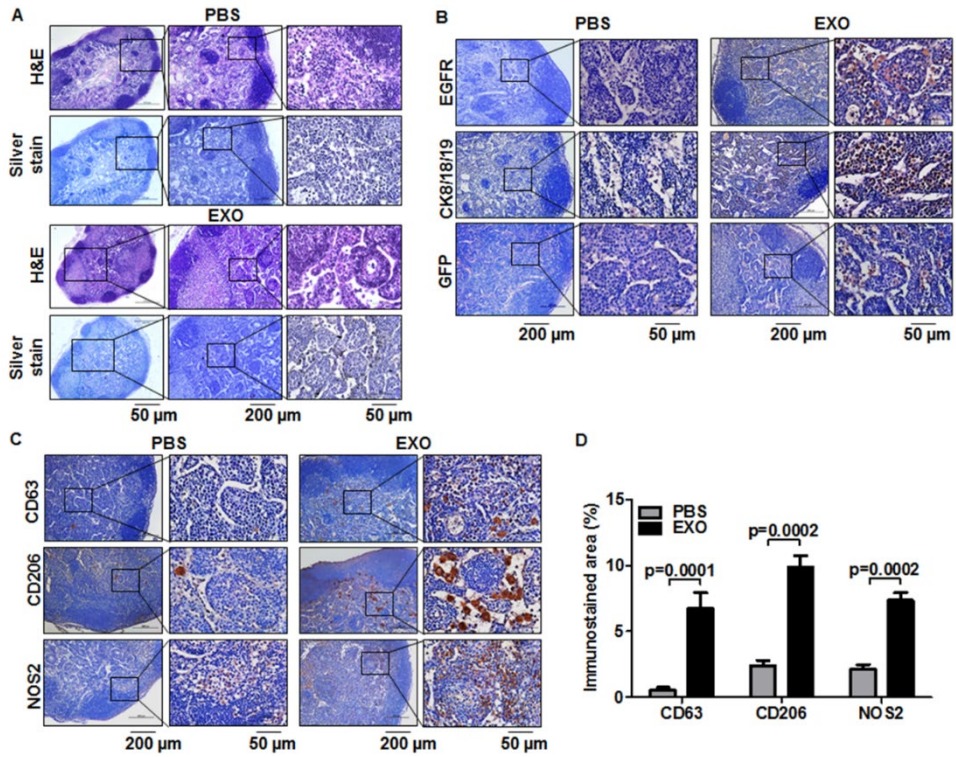

Figure 1-5. Histological analysis of axillary LN metastasis promoted by cancer cell-derived exosomes in TNBC models. After follow-up of tumor growth and axillary LN metastasis by use of biweekly BLI and US-guided PAI by intratumor injection with anti-EGFR-GNs, axillary LNs were isolated from tumor-bearing mice injected with RFP-tagged EXO or PBS. (A) H&E and silver staining images for the investigation of anti-EGFR-GNs accumulation in axillary LNs. (B). Immunostaining images of EGFR, CK18/8/19, and GFP for the evaluation of metastasis in axillary LNs. (C) Immunostaining images of CD206 and NOS2 for the evaluation of macrophage M2/M1 polarization in axillary LNs. Immunostaining images of CD63 for the analysis of exosome distribution in axillary LNs. (D) Quantitative immunostained area (mean ± S.E.) of CD63, CD206, and NOS2.

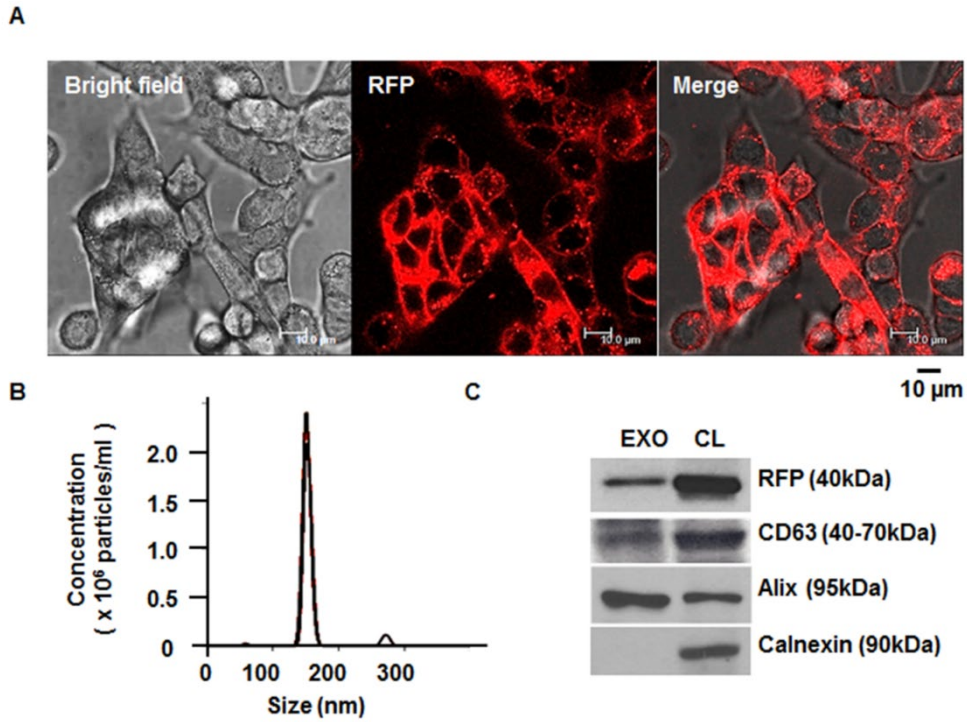

Figure 2-1. Generation of stable 4T1 cells expressing the exosomal CD63-RFP fusion protein and analysis of purified exosomes. (A) Confocal images of CD63-RFP-transduced 4T1 cells. Scale bar: 10 μm. (B) NanoSight analysis of the size and concentration of purified exosomes. (C) Western blot of RFP, CD63, Alix, and Calnexin in the purified exosomes (EXO) and the cell lysate (CL) of CD63-RFP-transduced 4T1 cells.

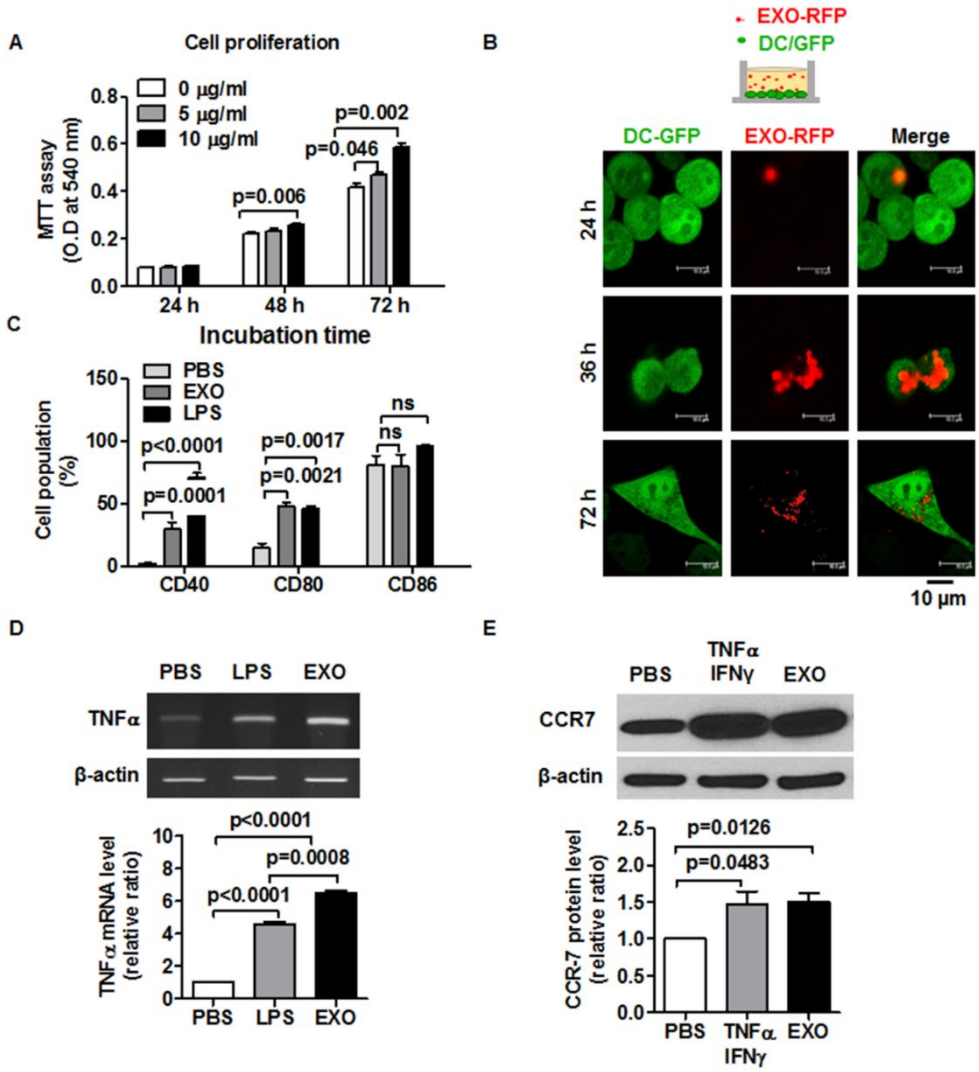
A
Cell proliferation
0 μg/ml
5 μg/ml
10 μg/ml
MTT assay (O.D at 540 nm)
0.8
0.6
0.4
0.2
0.0
p=0.002
p=0.046
p=0.006
24 h
48 h
72 h
Incubation time
B
EXO-RFP
DC/GFP
DC-GFP
EXO-RFP
Merge
24 h
36 h
72 h
10 μm
C
PBS
EXO
LPS
Cell population (%)
150
100
50
0
p<0.0001
p=0.0001
p=0.0017
p=0.0021
ns
ns
CD40
CD80
CD86
D
PBS
LPS
EXO
TNFα
β-actin
TNFα mRNA level (relative ratio)
10
8
6
4
2
0
p<0.0001
p=0.0008
p<0.0001
PBS
LPS
EXO
E
PBS
TNFα IFNγ
EXO
CCR7
β-actin
CCR-7 protein level (relative ratio)
2.5
2.0
1.5
1.0
0.5
0.0
p=0.0126
p=0.0483
PBS
TNFα IFNγ
EXO

Figure 2-2. Analysis of biological changes of exosome-stimulated DC2.4 cells. (A) MTT assay for evaluating the influence of EXO concentration and incubation time on DC2.4 cell proliferation. OD: optical density. (B) Confocal image of 4T1/CD63-RFP breast cancer cell-derived exosome (EXO-RFP) taken up by DC2.4 cells expressing G FP after administration of EXO -RFP (10 μg/ml) for 24-72 h. (C) Flow cytometry analysis of CD40, CD80, and CD86 on DC2.4 cells treated with EXO or LPS (100 ng/ml). (D) RT-PCR analysis of TNF-α mRNA levels from DC2.4 cells treated with EXO or LPS. (E) Western blot analysis of CCR7 protein levels from DC2.4 cells treated with EXO or TNF-α + IFN-γ (20 ng/ml). All experiments are performed in independent samples (n = 3) per group for each condition and repeated at least three times. All data are reported as the means $\pm$ S.E.

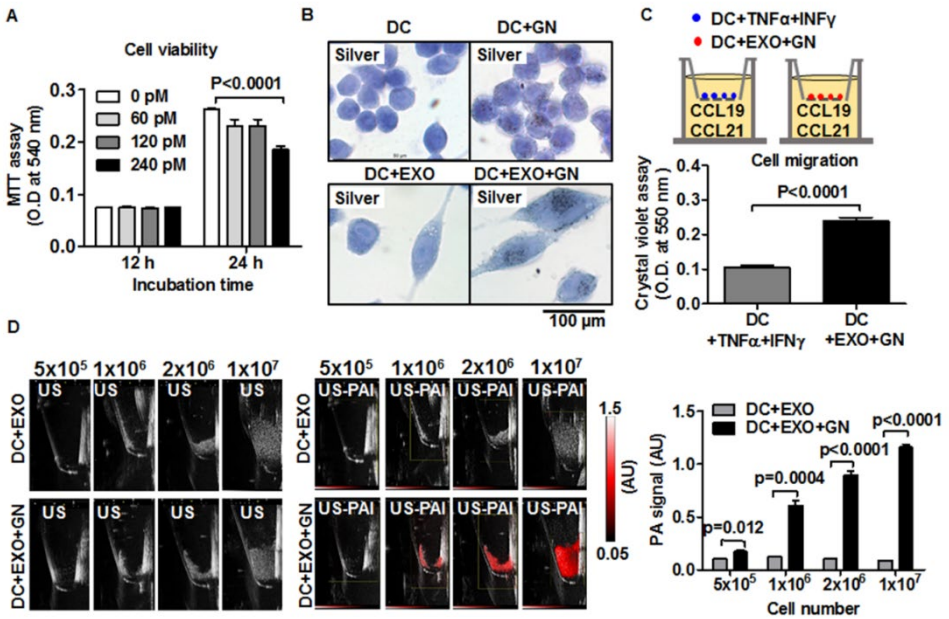

Figure 2-3. Analysis of in vitro US-guided PAI of GN-labeled DC2.4 cells. (A) MTT assay for evaluating the influence of GN concentration and labeling time on DC2.4 cell viability. OD: optical density. (B) Silver staining for detecting GNs uptaken by DC2.4 cells. (C) Transwell migratory assay of GN-labeled DC2.4 cells stimulated with EXO or TNF-α + IFN-γ (20 ng/ml) and stained with crystal violet. OD: optical density. (D) In vitro US-guided PAI analysis of EXO-stimulated and GN-labeled DC2.4 cells at different cell numbers. Fusion image (US-PAI) is obtained by overlaying a color-coded PA image on the top of the corresponding gray-scale US image. The unit for PA spectral measurement is an arbitrary unit (A.U.). The PA value in color bar ranges from 0.05 to 1.5 A.U. All experiments are performed in independent samples (n = 3) per group for each condition. All data are reported as the means ± S.E.

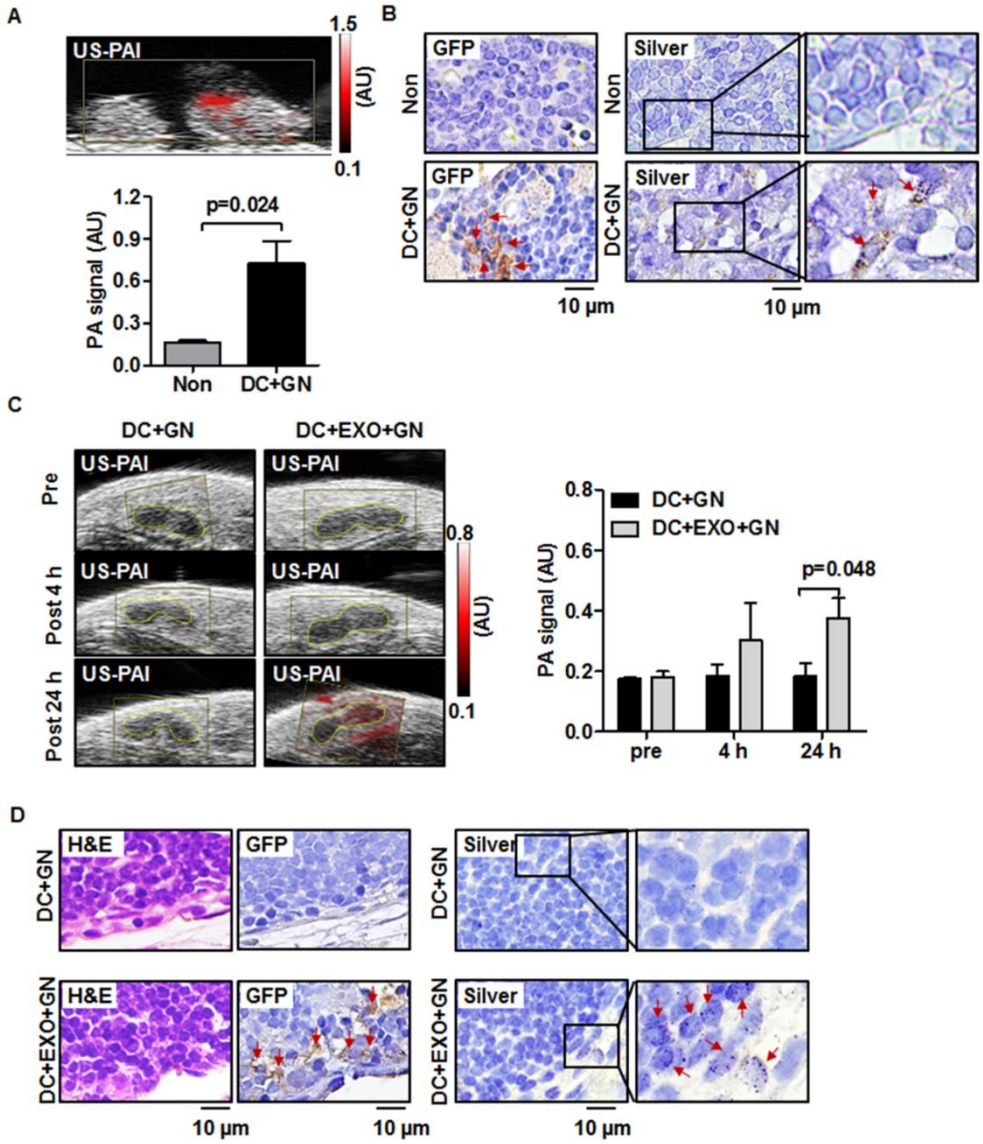
A
US-PAI
1.5
(AU)
0.1
PA signal (AU)
1.2
0.9
0.6
0.3
0.0
p=0.024
Non
DC+GN
B
GFP
Silver
Non
DC+GN
10 μm
C
DC+GN
DC+EXO+GN
Pre
Post 4 h
Post 24 h
US-PAI
0.8
0.1
DC+GN
DC+EXO+GN
p=0.048
pre
4 h
24 h
D
H&E
GFP
Silver
10 μm

Figure 2-4. US-guided PAI and histological analysis of exosome-stimulated and GN-labeled DC2.4 cell migration into LNs. (A) Ex vivo US-guided PAI analysis of GN-labeled DC2.4 cells directly injected into axillary LNs of three mice per each group. The unit for PA spectral measurement is an arbitrary unit (A.U.). The PA value in color bar ranges from 0.1 to 1.5 A.U. (B) GFP immunostaining and silver staining of the microsectioned axillary LNs with or without DC + GN injection. (C) *In vivo* US-guided PAI analysis of EXO-stimulated and GN-labeled DC2.4 cell migration into axillary LNs of five mice per each group before and at 4 h and 24 h after footpad injection. The unit for PA spectral measurement is an arbitrary unit (A.U.). The PA value in color bar ranges from 0.1 to 0.8 A.U. (D) H&E, GFP immunostaining, and silver staining of the microsectioned axillary LNs isolated from DC + GN and DC + EXO+GN mice at 24 h post-injection. Ex vivo and *in vivo* fusion image (US-PAI) is obtained by overlaying a color-coded PA image on the top of the corresponding gray-scale US image. All data are reported as the means ± S.E.

REFERENCES

1. Senkus E, Kyriakides S, Ohno S, Penault-Llorca F, Poortmans P, Rutgers E, Zackrisson S, Cardoso F, Committee EG: Primary breast cancer: ESMO Clinical Practice Guidelines for diagnosis, treatment and follow-up. *Ann Oncol* 2015, 26 Suppl 5:v8-30.
2. Bianchini G, Balko JM, Mayer IA, Sanders ME, Gianni L: Triple-negative breast cancer: challenges and opportunities of a heterogeneous disease. *Nat Rev Clin Oncol* 2016, 13(11):674-690.
3. Foulkes WD, Smith IE, Reis-Filho JS: Triple-negative breast cancer. *N Engl J Med* 2010, 363(20):1938-1948.
4. Kaufmann M, Rody A: Long-term risk of breast cancer recurrence: the need for extended adjuvant therapy. *J Cancer Res Clin Oncol* 2005, 131(8):487-494.
5. Raposo G, Stoorvogel W: Extracellular vesicles: exosomes, microvesicles, and friends. *J Cell Biol* 2013, 200(4):373-383.
6. Tickner JA, Urquhart AJ, Stephenson SA, Richard DJ, O'Byrne KJ: Functions and therapeutic roles of exosomes in cancer. *Front Oncol* 2014, 4:127.
7. Iero M, Valenti R, Huber V, Filipazzi P, Parmiani G, Fais S, Rivoltini L: Tumour-released exosomes and their implications in cancer immunity. *Cell Death Differ* 2008, 15(1):80-88.
8. Zhang HG, Grizzle WE: Exosomes: a novel pathway of local and distant intercellular communication that facilitates the

growth and metastasis of neoplastic lesions. *Am J Pathol* 2014, 184(1):28-41.

9. Mantovani A, Sozzani S, Locati M, Allavena P, Sica A: Macrophage polarization: tumor-associated macrophages as a paradigm for polarized M2 mononuclear phagocytes. *Trends Immunol* 2002, 23(11):549-555.

10. Hanahan D, Weinberg RA: Hallmarks of cancer: the next generation. *Cell* 2011, 144(5):646-674.

11. Quatromoni JG, Eruslanov E: Tumor-associated macrophages: function, phenotype, and link to prognosis in human lung cancer. *Am J Transl Res* 2012, 4(4):376-389.

12. Laoui D, Movahedi K, Van Overmeire E, Van den Bossche J, Schouppe E, Mommer C, Nikolaou A, Morias Y, De Baetselier P, Van Ginderachter JA: Tumor-associated macrophages in breast cancer: distinct subsets, distinct functions. *Int J Dev Biol* 2011, 55(7-9):861-867.

13. Sica A, Schioppa T, Mantovani A, Allavena P: Tumour-associated macrophages are a distinct M2 polarised population promoting tumour progression: potential targets of anti-cancer therapy. *Eur J Cancer* 2006, 42(6):717-727.

14. Cao W, Peters JH, Nieman D, Sharma M, Watson T, Yu J: Macrophage subtype predicts lymph node metastasis in oesophageal adenocarcinoma and promotes cancer cell invasion in vitro. *Br J Cancer* 2015, 113(5):738-746.

15. Zhang B, Cao M, He Y, Liu Y, Zhang G, Yang C, Du Y, Xu J, Hu J, Gao F: Increased circulating M2-like monocytes in patients

with breast cancer. *Tumour Biol* 2017, 39(6):1010428317711571.

16. Hollmen M, Roudnicky F, Karaman S, Detmar M: Characterization of macrophage--cancer cell crosstalk in estrogen receptor positive and triple-negative breast cancer. *Sci Rep* 2015, 5:9188.

17. Chow A, Zhou W, Liu L, Fong MY, Champer J, Van Haute D, Chin AR, Ren X, Gugiu BG, Meng Z *et al*: Macrophage immunomodulation by breast cancer-derived exosomes requires Toll-like receptor 2-mediated activation of NF-kappaB. *Sci Rep* 2014, 4:5750.

18. Su MJ, Aldawsari H, Amiji M: Pancreatic Cancer Cell Exosome-Mediated Macrophage Reprogramming and the Role of MicroRNAs 155 and 125b2 Transfection using Nanoparticle Delivery Systems. *Sci Rep* 2016, 6:30110.

19. Costa-Silva B, Aiello NM, Ocean AJ, Singh S, Zhang H, Thakur BK, Becker A, Hoshino A, Mark MT, Molina H *et al*: Pancreatic cancer exosomes initiate pre-metastatic niche formation in the liver. *Nat Cell Biol* 2015, 17(6):816-826.

20. Chen X, Ying X, Wang X, Wu X, Zhu Q, Wang X: Exosomes derived from hypoxic epithelial ovarian cancer deliver microRNA-940 to induce macrophage M2 polarization. *Oncol Rep* 2017, 38(1):522-528.

21. Wu L, Zhang X, Zhang B, Shi H, Yuan X, Sun Y, Pan Z, Qian H, Xu W: Exosomes derived from gastric cancer cells activate

NF-kappaB pathway in macrophages to promote cancer progression. *Tumour Biol* 2016, 37(9):12169-12180.

22. Ying X, Wu Q, Wu X, Zhu Q, Wang X, Jiang L, Chen X, Wang X: Epithelial ovarian cancer-secreted exosomal miR-222-3p induces polarization of tumor-associated macrophages. *Oncotarget* 2016, 7(28):43076-43087.

23. Jensen MM, Jorgensen JT, Binderup T, Kjaer A: Tumor volume in subcutaneous mouse xenografts measured by microCT is more accurate and reproducible than determined by 18F-FDG-microPET or external caliper. *BMC medical imaging* 2008, 8:16.

24. Wang LV, Gao L: Photoacoustic microscopy and computed tomography: from bench to bedside. *Annu Rev Biomed Eng* 2014, 16:155-185.

25. Zhang M, Kim HS, Jin T, Yi A, Moon WK: Ultrasound-guided photoacoustic imaging for the selective detection of EGFR-expressing breast cancer and lymph node metastases. *Biomed Opt Express* 2016, 7(5):1920-1931.

26. Takahashi Y, Nishikawa M, Shinotsuka H, Matsui Y, Ohara S, Imai T, Takakura Y: Visualization and in vivo tracking of the exosomes of murine melanoma B16-BL6 cells in mice after intravenous injection. *J Biotechnol* 2013, 165(2):77-84.

27. Eghtedari M, Oraevsky A, Copland JA, Kotov NA, Conjusteau A, Motamedi M: High sensitivity of in vivo detection of gold nanorods using a laser optoacoustic imaging system. *Nano letters* 2007, 7(7):1914-1918.

28. Luke GP, Yeager D, Emelianov SY: Biomedical applications of photoacoustic imaging with exogenous contrast agents. *Annals of biomedical engineering* 2012, 40(2):422-437.
29. Siphanto RI, Thumma KK, Kolkman RG, van Leeuwen TG, de Mul FF, van Neck JW, van Adrichem LN, Steenbergen W: Serial noninvasive photoacoustic imaging of neovascularization in tumor angiogenesis. *Optics express* 2005, 13(1):89-95.
30. Biswas SK, Sica A, Lewis CE: Plasticity of macrophage function during tumor progression: regulation by distinct molecular mechanisms. *J Immunol* 2008, 180(4):2011-2017.
31. Nishida-Aoki N, Tominaga N, Takeshita F, Sonoda H, Yoshioka Y, Ochiya T: Disruption of Circulating Extracellular Vesicles as a Novel Therapeutic Strategy against Cancer Metastasis. *Mol Ther* 2017, 25(1):181-191.
32. Vakkala M, Kahlos K, Lakari E, Paakko P, Kinnula V, Soini Y: Inducible nitric oxide synthase expression, apoptosis, and angiogenesis in in situ and invasive breast carcinomas. *Clin Cancer Res* 2000, 6(6):2408-2416.
33. Jia Y, Chen Y, Wang Q, Jayasinghe U, Luo X, Wei Q, Wang J, Xiong H, Chen C, Xu B *et al*: Exosome: emerging biomarker in breast cancer. *Oncotarget* 2017, 8(25):41717-41733.
34. Soki FN, Koh AJ, Jones JD, Kim YW, Dai J, Keller ET, Pienta KJ, Atabai K, Roca H, McCauley LK: Polarization of prostate cancer-associated macrophages is induced by milk fat globule-EGF factor 8 (MFG-E8)-mediated efferocytosis. *J Biol Chem* 2014, 289(35):24560-24572.

35. Maji S, Chaudhary P, Akopova I, Nguyen PM, Hare RJ, Gryczynski I, Vishwanatha JK: Exosomal Annexin II Promotes Angiogenesis and Breast Cancer Metastasis. *Mol Cancer Res* 2017, 15(1):93-105.
36. Menck K, Klemm F, Gross JC, Pukrop T, Wenzel D, Binder C: Induction and transport of Wnt 5a during macrophage-induced malignant invasion is mediated by two types of extracellular vesicles. *Oncotarget* 2013, 4(11):2057-2066.
37. Yang J, Zhang Z, Chen C, Liu Y, Si Q, Chuang TH, Li N, Gomez-Cabrero A, Reisfeld RA, Xiang R *et al*: MicroRNA-19a-3p inhibits breast cancer progression and metastasis by inducing macrophage polarization through downregulated expression of Fra-1 proto-oncogene. *Oncogene* 2014, 33(23):3014-3023.
38. Steinman RM, Banchereau J: Taking dendritic cells into medicine. *Nature* 2007, 449(7161):419-426.
39. Garg AD, Coulie PG, Van den Eynde BJ, Agostinis P: Integrating Next-Generation Dendritic Cell Vaccines into the Current Cancer Immunotherapy Landscape. *Trends Immunol* 2017, 38(8):577-593.
40. Anguille S, Smits EL, Lion E, van Tendeloo VF, Berneman ZN: Clinical use of dendritic cells for cancer therapy. *Lancet Oncol* 2014, 15(7):e257-267.
41. Gelao L, Criscitiello C, Esposito A, De Laurentiis M, Fumagalli L, Locatelli MA, Minchella I, Santangelo M, De Placido S, Goldhirsch A *et al*: Dendritic cell-based vaccines: clinical

applications in breast cancer. *Immunotherapy* 2014, 6(3):349-360.

42. Wu JM, Fackler MJ, Halushka MK, Molavi DW, Taylor ME, Teo WW, Griffin C, Fetting J, Davidson NE, De Marzo AM *et al*: Heterogeneity of breast cancer metastases: comparison of therapeutic target expression and promoter methylation between primary tumors and their multifocal metastases. *Clinical cancer research : an official journal of the American Association for Cancer Research* 2008, 14(7):1938-1946.

43. Thery C, Zitvogel L, Amigorena S: Exosomes: composition, biogenesis and function. *Nat Rev Immunol* 2002, 2(8):569-579.

44. Mahaweni NM, Kaijen-Lambers ME, Dekkers J, Aerts JG, Hegmans JP: Tumour-derived exosomes as antigen delivery carriers in dendritic cell-based immunotherapy for malignant mesothelioma. *J Extracell Vesicles* 2013, 2.

45. Wolfers J, Lozier A, Raposo G, Regnault A, Thery C, Masurier C, Flament C, Pouzieux S, Faure F, Tursz T *et al*: Tumor-derived exosomes are a source of shared tumor rejection antigens for CTL cross-priming. *Nat Med* 2001, 7(3):297-303.

46. Andre F, Schartz NE, Chaput N, Flament C, Raposo G, Amigorena S, Angevin E, Zitvogel L: Tumor-derived exosomes: a new source of tumor rejection antigens. *Vaccine* 2002, 20 Suppl 4:A28-31.

47. Clayton A, Mason MD: Exosomes in tumour immunity. *Curr Oncol* 2009, 16(3):46-49.
48. Alloatti A, Kotsias F, Magalhaes JG, Amigorena S: Dendritic cell maturation and cross-presentation: timing matters! *Immunol Rev* 2016, 272(1):97-108.
49. Cho JA, Yeo DJ, Son HY, Kim HW, Jung DS, Ko JK, Koh JS, Kim YN, Kim CW: Exosomes: a new delivery system for tumor antigens in cancer immunotherapy. *Int J Cancer* 2005, 114(4):613-622.
50. Santos PM, Butterfield LH: Dendritic Cell-Based Cancer Vaccines. *J Immunol* 2018, 200(2):443-449.
51. Ntziachristos V: Going deeper than microscopy: the optical imaging frontier in biology. *Nat Methods* 2010, 7(8):603-614.
52. Weber J, Beard PC, Bohndiek SE: Contrast agents for molecular photoacoustic imaging. *Nat Methods* 2016, 13(8):639-650.
53. Li W, Chen X: Gold nanoparticles for photoacoustic imaging. *Nanomedicine (Lond)* 2015, 10(2):299-320.
54. Lee SB, Lee YJ, Cho SJ, Kim SK, Lee SW, Lee J, Lim DK, Jeon YH: Antigen-Free Radionuclide-Embedded Gold Nanoparticles for Dendritic Cell Maturation, Tracking, and Strong Antitumor Immunity. *Adv Healthc Mater* 2018, 7(9):e1701369.
55. Libutti SK, Paciotti GF, Byrnes AA, Alexander HR, Jr., Gannon WE, Walker M, Seidel GD, Yuldasheva N, Tamarkin L: Phase I and pharmacokinetic studies of CYT-6091, a novel PEGylated

colloidal gold–rhTNF nanomedicine. *Clinical cancer research : an official journal of the American Association for Cancer Research* 2010, 16(24):6139–6149.

56. Kharlamov AN, Tyurnina AE, Veselova VS, Kovtun OP, Shur VY, Gabinsky JL: Silica–gold nanoparticles for atheroprotective management of plaques: results of the NANOM–FIM trial. *Nanoscale* 2015, 7(17):8003–8015.

57. Pedrosa P, Vinhas R, Fernandes A, Baptista PV: Gold Nanotheranostics: Proof–of–Concept or Clinical Tool? *Nanomaterials (Basel)* 2015, 5(4):1853–1879.

58. Aslakson CJ, Miller FR: Selective events in the metastatic process defined by analysis of the sequential dissemination of subpopulations of a mouse mammary tumor. *Cancer Res* 1992, 52(6):1399–1405.

59. Shen Z, Reznikoff G, Dranoff G, Rock KL: Cloned dendritic cells can present exogenous antigens on both MHC class I and class II molecules. *J Immunol* 1997, 158(6):2723–2730.

60. Hwang DW, Choi H, Jang SC, Yoo MY, Park JY, Choi NE, Oh HJ, Ha S, Lee YS, Jeong JM *et al*: Noninvasive imaging of radiolabeled exosome–mimetic nanovesicle using (99m)Tc–HMPAO. *Sci Rep* 2015, 5:15636.

61. Livak KJ, Schmittgen TD: Analysis of relative gene expression data using real–time quantitative PCR and the 2(–Delta Delta C(T)) Method. *Methods* 2001, 25(4):402–408.

62. Luke GP, Nam SY, Emelianov SY: Optical wavelength selection for improved spectroscopic photoacoustic imaging. *Photoacoustics* 2013, 1(2):36-42.

63. Zeelenberg IS, Ostrowski M, Krumeich S, Bobrie A, Jancic C, Boissonnas A, Delcayre A, Le Pecq JB, Combadiere B, Amigorena S *et al*: Targeting tumor antigens to secreted membrane vesicles in vivo induces efficient antitumor immune responses. *Cancer Res* 2008, 68(4):1228-1235.

64. Jang JY, Lee JK, Jeon YK, Kim CW: Exosome derived from epigallocatechin gallate treated breast cancer cells suppresses tumor growth by inhibiting tumor-associated macrophage infiltration and M2 polarization. *BMC Cancer* 2013, 13:421.

65. Yu S, Liu C, Su K, Wang J, Liu Y, Zhang L, Li C, Cong Y, Kimberly R, Grizzle WE *et al*: Tumor exosomes inhibit differentiation of bone marrow dendritic cells. *J Immunol* 2007, 178(11):6867-6875.

66. Ning Y, Shen K, Wu Q, Sun X, Bai Y, Xie Y, Pan J, Qi C: Tumor exosomes block dendritic cells maturation to decrease the T cell immune response. *Immunol Lett* 2018, 199:36-43.

67. Piao YJ, Kim HS, Hwang EH, Woo J, Zhang M, Moon WK: Breast cancer cell-derived exosomes and macrophage polarization are associated with lymph node metastasis. *Oncotarget* 2018, 9(7):7398-7410.

68. Trevejo JM, Marino MW, Philpott N, Josien R, Richards EC, Elkon KB, Falck-Pedersen E: TNF-alpha -dependent maturation of local dendritic cells is critical for activating the

adaptive immune response to virus infection. *Proc Natl Acad Sci U S A* 2001, 98(21):12162-12167.

69. Clatworthy MR, Aronin CE, Mathews RJ, Morgan NY, Smith KG, Germain RN: Immune complexes stimulate CCR7-dependent dendritic cell migration to lymph nodes. *Nat Med* 2014, 20(12):1458-1463.

70. Gu X, Erb U, Buchler MW, Zoller M: Improved vaccine efficacy of tumor exosome compared to tumor lysate loaded dendritic cells in mice. *Int J Cancer* 2015, 136(4):E74-84.

71. De Vries IJ, Krooshoop DJ, Scharenborg NM, Lesterhuis WJ, Diepstra JH, Van Muijen GN, Strijk SP, Ruers TJ, Boerman OC, Oyen WJ *et al*: Effective migration of antigen-pulsed dendritic cells to lymph nodes in melanoma patients is determined by their maturation state. *Cancer Res* 2003, 63(1):12-17.

72. Aarntzen EH, Srinivas M, Bonetto F, Cruz LJ, Verdijk P, Schreibelt G, van de Rakt M, Lesterhuis WJ, van Riel M, Punt CJ *et al*: Targeting of 111In-labeled dendritic cell human vaccines improved by reducing number of cells. *Clinical cancer research : an official journal of the American Association for Cancer Research* 2013, 19(6):1525-1533.

73. Prince HM, Wall DM, Ritchie D, Honemann D, Harrrison S, Quach H, Thompson M, Hicks R, Lau E, Davison J *et al*: In vivo tracking of dendritic cells in patients with multiple myeloma. *J Immunother* 2008, 31(2):166-179.

74. Lee SB, Lee HW, Lee H, Jeon YH, Lee SW, Ahn BC, Lee J, Jeong SY: Tracking dendritic cell migration into lymph nodes

by using a novel PET probe (18)F-tetrafluoroborate for sodium/iodide symporter. *EJNMMI Res* 2017, 7(1):32.

75. Adonai N, Adonai N, Nguyen KN, Walsh J, Iyer M, Toyokuni T, Phelps ME, McCarthy T, McCarthy DW, Gambhir SS: Ex vivo cell labeling with 64Cu-pyruvaldehyde-bis(N4-methylthiosemicarbazone) for imaging cell trafficking in mice with positron-emission tomography. *Proc Natl Acad Sci U S A* 2002, 99(5):3030-3035.

76. de Vries IJ, Lesterhuis WJ, Barentsz JO, Verdijk P, van Krieken JH, Boerman OC, Oyen WJ, Bonenkamp JJ, Boezeman JB, Adema GJ *et al*: Magnetic resonance tracking of dendritic cells in melanoma patients for monitoring of cellular therapy. *Nat Biotechnol* 2005, 23(11):1407-1413.

77. Joo HJ, Kim HS, Choi YS, Kim H, Kim SJ, Moon WK: Detection of prostaglandin E2-induced dendritic cell migration into the lymph nodes of mice using a 1.5 T clinical MR scanner. *NMR Biomed* 2012, 25(4):570-579.

78. Noh YW, Lim YT, Chung BH: Noninvasive imaging of dendritic cell migration into lymph nodes using near-infrared fluorescent semiconductor nanocrystals. *FASEB J* 2008, 22(11):3908-3918.

79. Pham W, Xie J, Gore JC: Tracking the migration of dendritic cells by in vivo optical imaging. *Neoplasia* 2007, 9(12):1130-1137.

80. Su H, Mou Y, An Y, Han W, Huang X, Xia G, Ni Y, Zhang Y, Ma J, Hu Q: The migration of synthetic magnetic nanoparticle

labeled dendritic cells into lymph nodes with optical imaging. *Int J Nanomedicine* 2013, 8:3737–3744.

국문초록

서론: 암세포 유래 엑소좀은 면역세포와의 정보교환을 통해 종양면역을 조절하여 암의 진행과 전이에 관여한다고 알려져 있지만 유방암에서 엑소좀의 자극을 받은 대식세포 또는 수지상세포의 면역기능 변화가 암 진행과 전이에 주는 영향에 관한 생체 연구는 부족하다. 따라서 본 연구에서는 세포추적 영상으로 유방암세포유래 엑소좀과 대식세포 또는 수지상세포와의 상호작용을 관찰하고 엑소좀에 의한 대식세포와 수지상세포의 종양면역 기능 변화를 분석하고자 한다. 또한 생체광학영상기법과 일체형 광음향 초음파 영상기법을 이용하여 엑소좀에 의한 유방암 진행과 전이 기전을 규명하고자 한다.

실험방법: 본 연구에서는 사람과 마우스 삼중음성유방암세포(MDA-MB-231과 4T1), 마우스 대식세포(Raw264.7) 그리고 마우스 수지상세포(DC2.4)를 사용하였다. 렌티바이러스 시스템을 이용해 엑소좀 특이 막단백질(CD63)과 적색형광단백질(RFP)를 재조합한 CD63/RFP를 발현하는 MDA-MB-231-CD63/RFP, 4T1-CD63/RFP, 루시퍼라제(firefly luciferase)와 녹색형광단백질(GFP)을 동시에 발현하는 MDA-MB-231-Luc/GFP, GFP를 발현하는 RAW264.7/GFP와 DC2.4/GFP를 수립하였다. MDA-MB-231-CD63/RFP 와 4T1-CD63/RFP에서

분비되는 적색형광단백질을 발현하는 엑소좀을 추출하여, 나노입자분석기기(NanoSight)를 사용하여 크기를 측정하고, 웨스턴 블럿으로 엑소좀 특이 단백질의 발현을 확인하였다. 추출한 엑소좀의 세포간 이동을 공초점 현미경으로 추적 관찰하였으며, 세포증식 평가(MTT)와 트렌스웰 이동 분석법으로 엑소좀에 의한 세포들의 증식, 이동 및 침윤 능력을 분석하였고, 실시간 역전사중합효소연쇄반응법, 웨스턴 블럿과 유세포 분석으로 대식세포와 수지상세포의 면역기능을 분석하였다. 면역결핍마우스(BALB/c nude)의 유선지방조직에 MDA-MB-231-Luc/GFP를 이식하여 유방암모델을 만들었다. 생체발광영상으로 엑소좀에 의한 종양의 성장과 전이 과정을 추적 관찰하였고 일체형 광음향 초음파 영상으로 EGFR항체가 탑재된 골드나노로드(anti-EGFR-GNs)를 일차 종양에 주입하여 유방암 림프절 전이를 분석하였다. 또한 마우스 피하에 엑소좀으로 활성시킨 수지상세포를 골드나노로드(GNs)로 표지하여 주사하고 피하부터 액와림프절로의 이동을 일체형 광음향 초음파 영상기법으로 추적 관찰 하였다. 영상 분석 후 적출한 종양 및 림프절 조직에서 H&E염색과 면역염색을 수행하였다.

결과: 유방암세포, 대식세포 그리고 수지상세포내에서 유방암세포 유래 엑소좀의 포식을 확인하였고 그 중 대식세포와 수지상세포는 엑소좀에 의해 활성화 되는 것이 관찰되었다. 엑소좀에 의해 각 세포들의 성장, 이동 및 침윤 능력이 증가되었고, 대식세포에서는 M1, M2 분극화 발현

마커인 NOS2와 CD206, Arginase-1의 발현이 유도되었고, 수지상세포에서는 보조자극 분자인 CD40, CD80, CD86의 발현과 이동성 관련 케모카인 수용체인 CCR7의 발현뿐만 아니라 분화와 성숙을 자극하는 TNF-α의 발현이 증가되었다. 생체발광영상과 일체형 광음향 초음파 영상으로 유방암 모델에서 엑소좀에 의해 종양의 성장과 전이가 촉진되는 것을 확인하였고 마우스의 피하에 이식한 엑소좀으로 활성 된 수지상세포는 림프절로의 이동 능력이 증가되었다.

결론: 형광단백질을 발현하는 유방암세포 유래의 엑소좀이 유방암세포, 대식세포, 수지상세포로 이동하는 과정을 실시간으로 추적 관찰한 결과, 엑소좀은 대식세포의 분극화와 수지상세포의 분화를 유도하여 유방암의 성장과 전이를 조절할 것이라는 가능성을 제시하였다. 또한 생체광학영상기법과 일체형 광음향 초음파 영상기법은 엑소좀에 의한 국소 림프절 전이 여부와 수지상세포의 이동과 분포를 효율적으로 추적 관찰하고, 분석할 수 있는 생체 영상법으로 다양한 암종에 활용에 활용될 수 있을 것이다.

주요어: 삼중음성유방암, 엑소좀, 림프절, 암 전이, 대식세포, 수지상세포, 광음향 초음파 영상, 골드나노로드

학번: 2015-22409